2016

Small punch test simulation of laminated magnesium alloy composite with aluminum/silicon carbide pattern-reinforcement

Miao Liu
Iowa State University

Small punch test simulation of laminated magnesium alloy composite with aluminum/silicon carbide pattern-reinforcement

by

Miao Liu

A thesis submitted to the graduate faculty

in partial fulfillment of the requirements for the degree of

MASTER OF SCIENCE

Major: Mechanical Engineering

Program of Study Committee:
Gap-Yong Kim, Major Professor
Pranav Shrotriya
Wei Hong

Iowa State University

Ames, Iowa

2016

TABLE OF CONTENTS

ACKNOWLEDGEMENTS

First of all, I would like to thank my major professor, Dr. Gap-Yong Kim, for his guidance, support and patience. In addition, I would also like to offer my appreciation for the great amount of help from my colleagues, Mina Bastwros and Saeed Mousa, without them, this work would not have been possible. Finally, thanks to all the faculties and friend in our department for making this such a good journey in Iowa State University.

ABSTRACT

Metal matrix composites (MMCs) have been widely used in various industries including aerospace, automotive, transportation, etc. While many types of MMCs have been studied and developed, including reinforcement phases of mono filaments, short/long fibers, and particles, their arrangement within the matrix has been rather simple. In this study, a finite element simulation tool has been used to study laminate composites with complex configurations. A finite element analysis has been performed to understand the strengthening effect of pattern-reinforced composite structure using a small punch test. It was found that the pattern reinforcement helped to distribute stress and strain during deformation. This resulted in the strength increase of 40% when compared with a uniform alternating layer-reinforced composite. Furthermore, composites with three different pattern sizes of 2 μm, 20 μm and 50 μm with the same reinforcement loading were compared. The smallest pattern showed the highest strength compared with larger patterns by 30% and 60%. Furthermore, the influence of elastic modulus, yield strength, ultimate strength, and fracture strain on the four deformation stages of the small punch test has been analyzed. Based on the analysis, a modified energy dissipation equation was developed to compensate for variations originating from the sheet thickness and the test ball size. This study helps to explain the strengthening effect from a pattern-reinforced laminate composite in comparison with the uniform alternating layer-reinforced structure. It demonstrated potential ways to alter or tailor mechanical properties of laminate composites and to further optimize the configuration of custom designed laminate composites.

CHAPTER 1. INTRODUCTION

1.1 Motivation

Metal matrix composites (MMCs) have drawn a significant amount of interest since the 1980s due to their favorable mechanical, thermal, and electrical properties [1]. They are widely applied in aerospace, automotive, and other industrial fields. While many types of MMCs have been studied and developed, including reinforcement phases of mono filaments, short/long fibers, and particles, their arrangement within the matrix has been rather simple. In this study, a finite element simulation tool is used to study composites with complex configuration. A pattern-reinforced magnesium alloy composite fabricated by sintering laminated sheets is modeled and simulated to understand the strengthening effects. A magnesium alloy, AZ31, is used as the matrix, and the reinforcement phase has a circular pattern structure made of SiCp/Al6061p. The simulation is performed to understand the strengthening effect of the pattern-reinforced composite in comparison to a laminated composite with alternating layers. The small punch test (SPT) is employed to test the fabricated composite and the results are compared with simulation outcomes.

1.2 Research Framework and Objectives

The goals of this study are: (1) to analyze the SPT through finite element analysis (FEA), and (2) to understand the strengthening effects of pattern-reinforced laminate metal composites. First, the governing stress and strain evolution during the SPT is analyzed to understand the force vs displacement behavior of bulk metallic material during the test. Next, a simulation tool is utilized to analyze the failure of laminate and pattern-reinforced composites.

1.2.1 Simulation of Small Punch Test and Analysis of Stress and Strain Evolution

In this section, simulation of the SPT is verified by comparing the force response in experiments and numerical analysis. Then, the material stress and strain during the SPT is analyzed to understand the behavior of the force vs displacement curve. Using the FEA tool, the effects of yield strength, ultimate strength, fracture strain, and Young's modulus on the loading curve is investigated. The energy dissipation in the SPT is correlated with tensile mode energy dissipation, and a modified equation is proposed to eliminate the punch size and specimen thickness effects.

1.2.2 Small Punch Test Simulation of Uniform Layer-Reinforced and Pattern-Reinforced Laminated Metal Composites

This section presents a numerical investigation of the performance of the pattern-reinforced composite by comparing it with a uniform layer-reinforced composite. The composite material properties used in the FEA model are verified in the experiment. A model with increased pattern thickness is analyzed for its effects on strength. The pattern thickness effect on the material strengthening is explained with the FEA model.

CHAPTER 2. SIMULATION OF THE SMALL PUNCH TEST AND ANALYSIS OF STRESS AND STRAIN EVOLUTION

In this chapter, the SPT is analyzed using a finite element simulation tool. First, the model is validated with the experimental results and then employed to analyze the specimen deformation during the test. Then the effects of material yield strength, ultimate strength, fracture strain, and Young's modulus on the force vs. displacement curve are analyzed.

2.1 Introduction and Background of the Small Punch Test

The SPT is a powerful way to test miniaturized specimens because it only requires a small amount of material. The device consists of a ceramic punch ball with a small radius and dies to secure the specimen. A constant displacement per unit time is applied to the punch, which is placed at the center of the specimen until it is penetrated or until the disc completely loses the ability to hold any load. The SPT setup is shown in Figure 1.

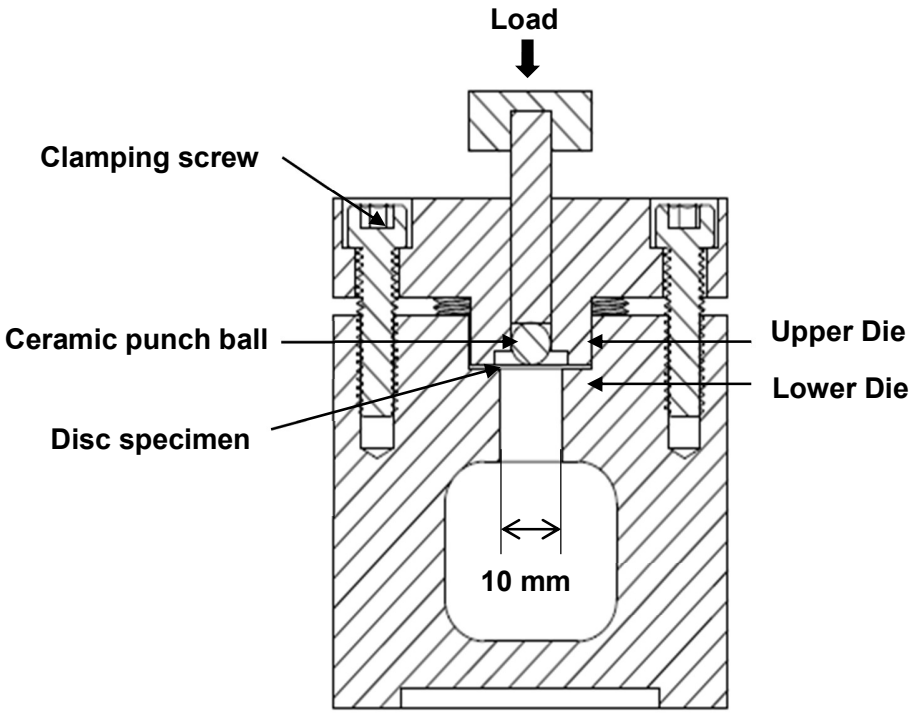

Figure 1. Schematic of the SPT

The test was first developed as a miniaturized disc bend test to determine the post-irradiation mechanical properties of materials used in a nuclear environment [2]. The SPT, which only requires a small amount of material, was an alternative developed to test the material properties of a limited number of irradiated standard specimens in the 1980s [3]. It was further developed and used as a measurement tool to test mechanical properties of ductile tensile materials in recent decades. The test is still a nonstandard test but is useful for measuring small-piece specimens that do not lend themselves to other standard ways of testing and for extracting material mechanical properties from limited amounts of material. The SPT may be performed in two ways. One uses a constant displacement per unit time where the punch is given at a constant rate of motion and the force is measured through a sensor. The other uses a constant force applied on the punch. The displacement with time dependency is analyzed. The empirical

standards correlations of the test has been well established between the experimental data with material tensile properties [4-8]. Through the material performance as seen from the SPT, material properties such as elastic modulus, fracture toughness, and tensile strength can be extracted [4, 9, 10]. A study that used the SPT to analyze fracture properties for different specimen thicknesses showed that the properties significantly depended on the thickness of the specimen [11]. The temperature of the specimen when subjected to the SPT also had a large influence on the behavior of the material [12].

As the SPT became more popular, FEA tools were employed for analysis [11, 13-15]. The FEA model has been used to calculate the stress state in a specimen disc. However, there is limited work on using the SPT to analyze composite materials. Composite materials behave differently than homogenous materials, and therefore conventional knowledge of homogenous materials may not apply. During the actual SPT, the rupture time and the rupture initiation position is almost impossible to observe. The specimens used in the SPT are laminated sheets with mesoscale patterns which consist of nanoscale particles.

2.2 Experimental Setup

The SPT device consists of a bottom die, a top die, a ceramic punch ball, a shaft, and a top cap where the load is applied. The screws on the top die apply downward pressure when they are tightened so that the top die clamps the disc. The center hole of the bottom die has a diameter of 10 mm. The center hole of the top die has a diameter of 12 mm. The disc specimen is 19 mm and is placed in the bottom die, which has a diameter of 20 mm. The punch ball is 6.35 mm in diameter. The displacement rate of the punch ball is set at 0.05 mm/s. Displacement and force are both recorded during the test. Figure 2 shows the setup of the actual experiment.

Figure 2. Actual SPT device

2.3 FEA Model

We employed Abaqus 6.13 as the FEA tool to conduct the simulation. The simulation followed the settings used in the actual experiment and used the material properties from the tensile test.

2.3.1 Boundary Conditions

In the FEA model, boundary conditions were set in order to achieve the same setup during the experiment. Figure 3 shows an exploded view of the FEA model.

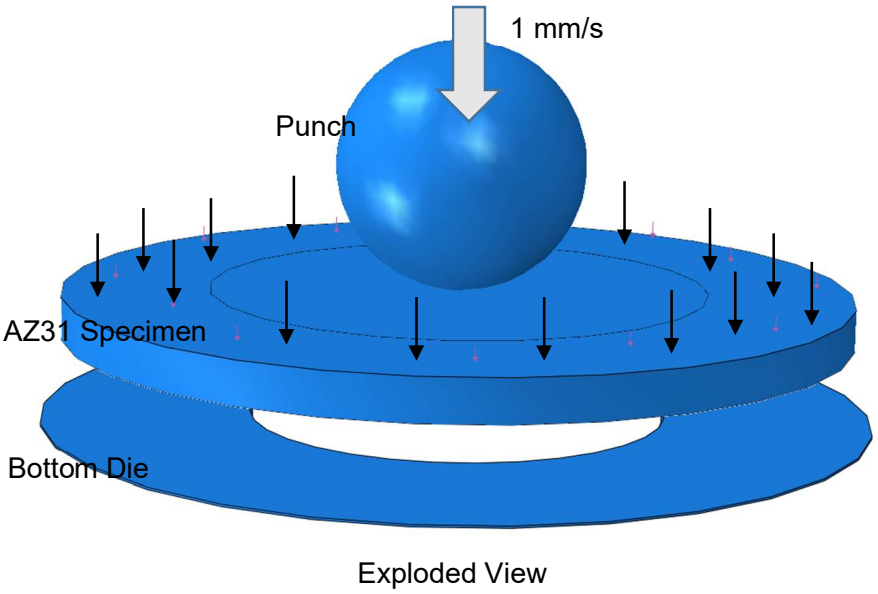

Figure 3. FEA model setup for SPT

The bottom die had an inner hole of 10 mm and was fixed at all degrees of freedom. The top surface of the specimen disc was partitioned with a circle 12 mm in diameter. Pressure of 10 MPa was applied downward on the ring area on the AZ31 specimen to the clamped disc. The friction coefficient between the disc and the bottom die was 0.3. Both the punch and the bottom die were rigid. The punch moved toward the disc at a speed of 1 mm/s. Since the strain rate effect was not included as a material property, a higher punch speed was set for the purpose of efficiency.

2.3.2 Material Properties

The as-received AZ31 was tested with the SPT. A tensile test was also performed on the as-received AZ31 with ASTM standard to obtain the tensile material properties for use with the FEA. The tensile property is shown in Figure 4. Based on the experimental data, the Young's

modulus was observed to be 15 GPa. The Poisson's ratio was 0.33, derived from specification sheets of the material.

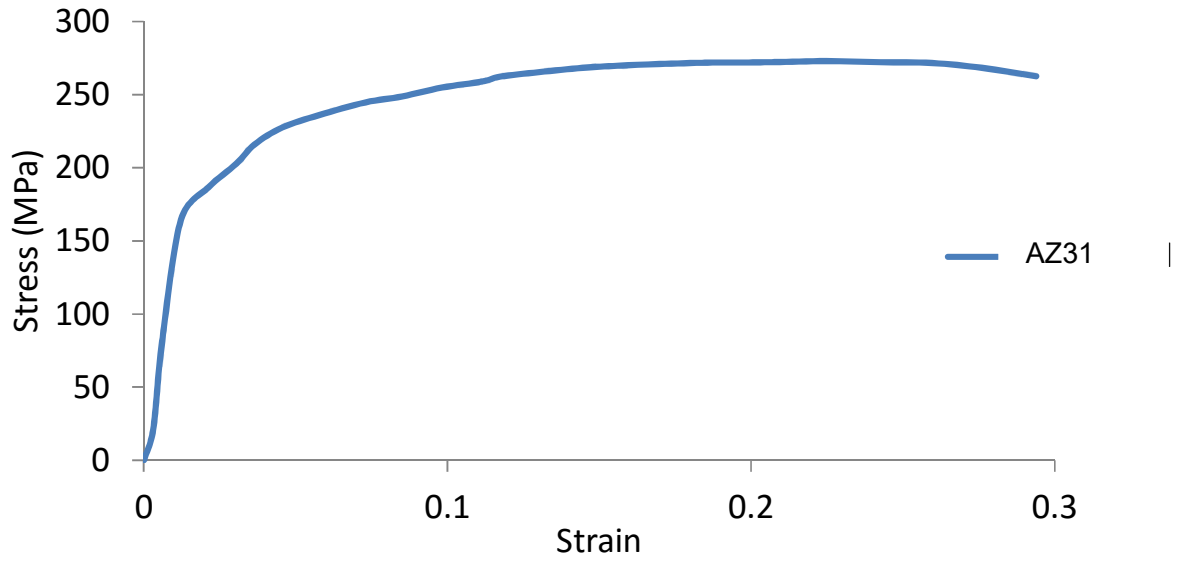

Figure 4. Engineering stress vs. strain curve of the AZ31 tensile test

Table 1. Isotropic hardening data for the AZ31 (true stress)

Yield stress (MPa)	167.5	190	262	299	316	334	338
Plastic Strain	0	0.008	0.06	0.11	0.14	0.19	0.20

The model used ductile damage settings to define the material fracture behavior. The fracture strain was defined in the settings and Figure 5 shows how Abaqus defined the fracture strain. Once the plastic strain of the elements in the model entered the zone of fracture strain in Figure 5, the element started to degrade and failed.

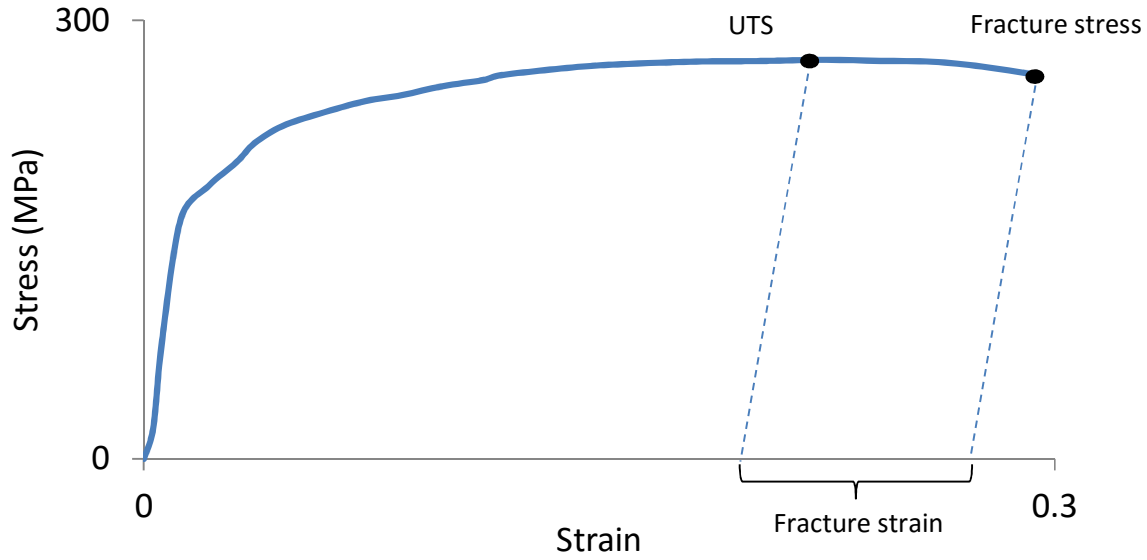

Figure 5. Fracture strain defined in Abaqus

The material failed due to the growth of degradation of material stiffness, which was defined as damage evolution in the damage setting. Plastic displacement was chosen to drive the evolution of the damage, which was related to the size of the element. The plastic displacement was approximately equal to the fracture strain times the characteristic length of the element.

2.3.3 Mesh

The FEA model of the disc specimen was meshed to 8-node solid elements with reduced integration (C3D8R) elements. The mesh of the model is shown in Figure 6.

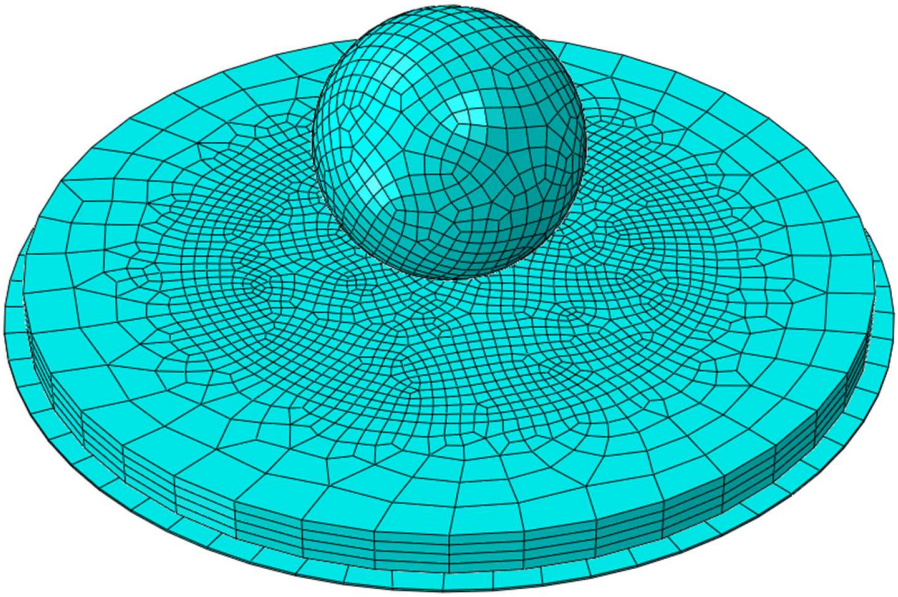

Figure 6. Mesh generation of the FEA model

To simplify the numerical analysis, the center of the disc used a mesh size of 0.3 and a larger mesh size of 1.5 was generated for the outer area. A total of 10,000 nodes were used in the disc and 8300 elements were used.

2.4 Results and Discussion

2.4.1 Numerical Simulation Validation

The actual SPT data validated the FEA model. The shapes of parts from the SPT are compared in Figure 7. The predicted of location of the rupture is in a good agreement with actual disk deformed in the experiment.

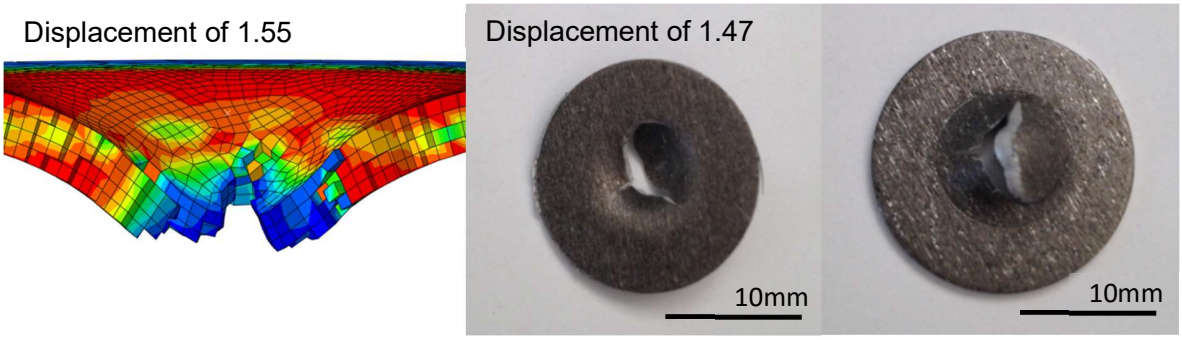

Figure 7. Comparison of parts in both the FEA modeling and the actual experiment

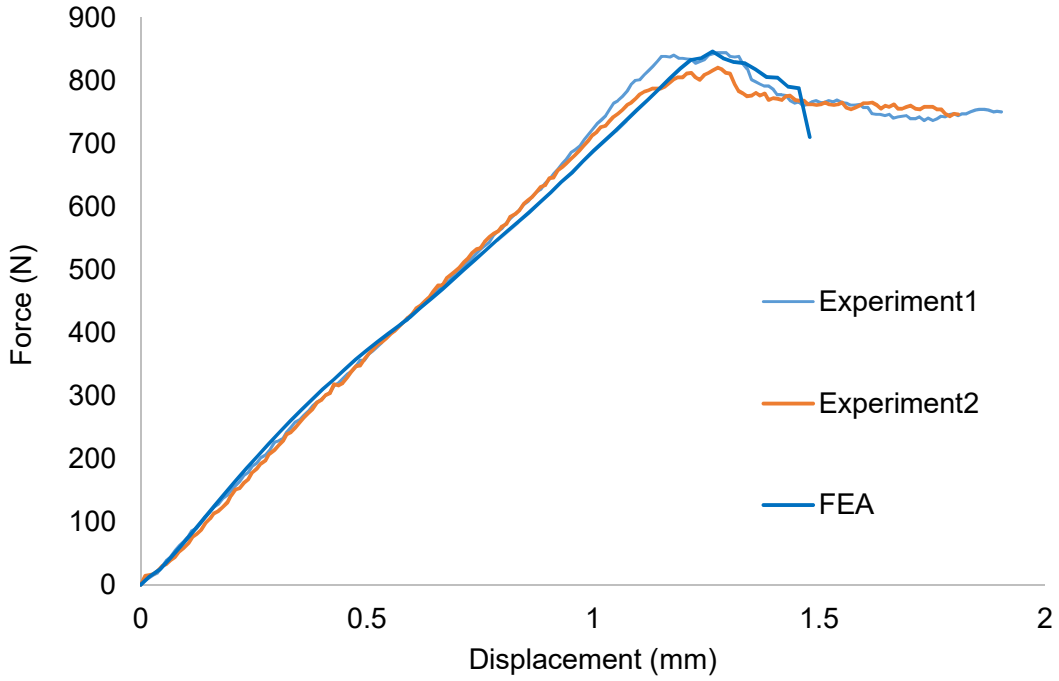

Figure 8. Force vs displacement curve of the as-received AZ31 specimen

The force and displacement curves from the simulation and the experiments are compared in Figure 8. The load values were within 5%, and the prediction of failure strain was in good agreement. Overall, the results from the simulation and the experiments closely matched. The model could now be further utilized in the analysis.

2.4.2 Force vs Displacement Curve Analysis

A typical force vs displacement curve is divided into four regions, as shown in Figure 9. Region I shows the elastic bending deformation, which is related to local yielding and dominated by the yield strength and elastic modulus of the material. Region II shows the plastic bending deformation. This region goes through plastic deformation during the test. Region III involves membrane stretching. The last region shows the plastic instability, where the disc completely fails [11].

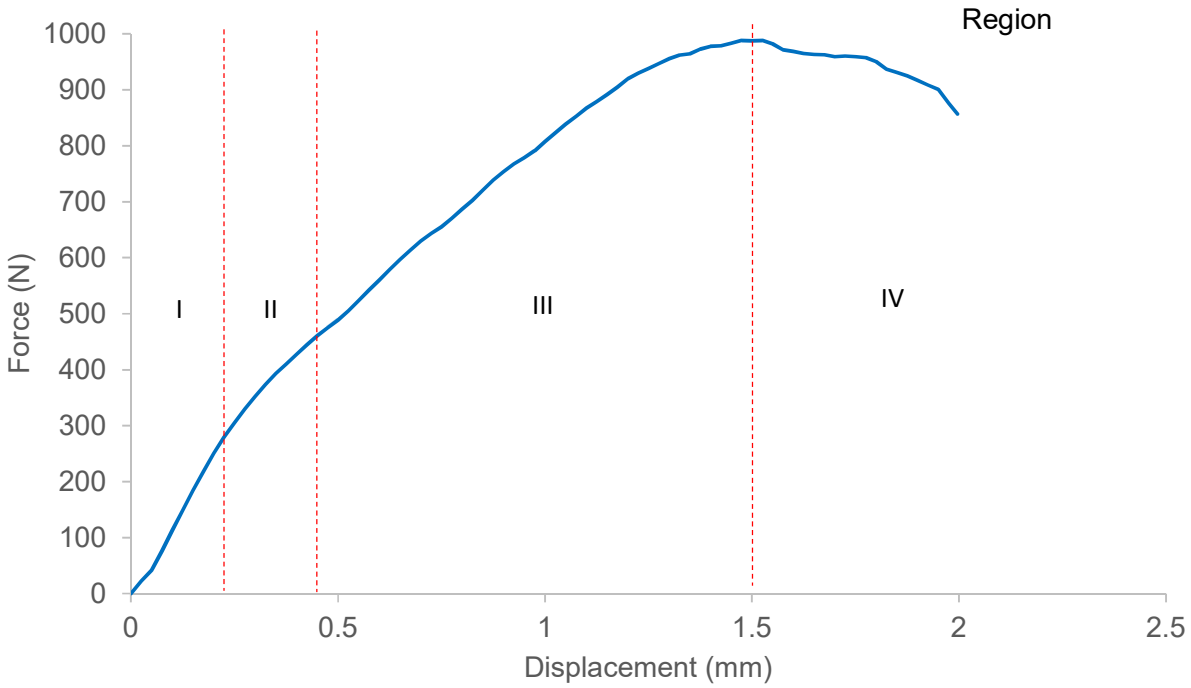

Figure 9. Typical force vs. displacement curve [16]

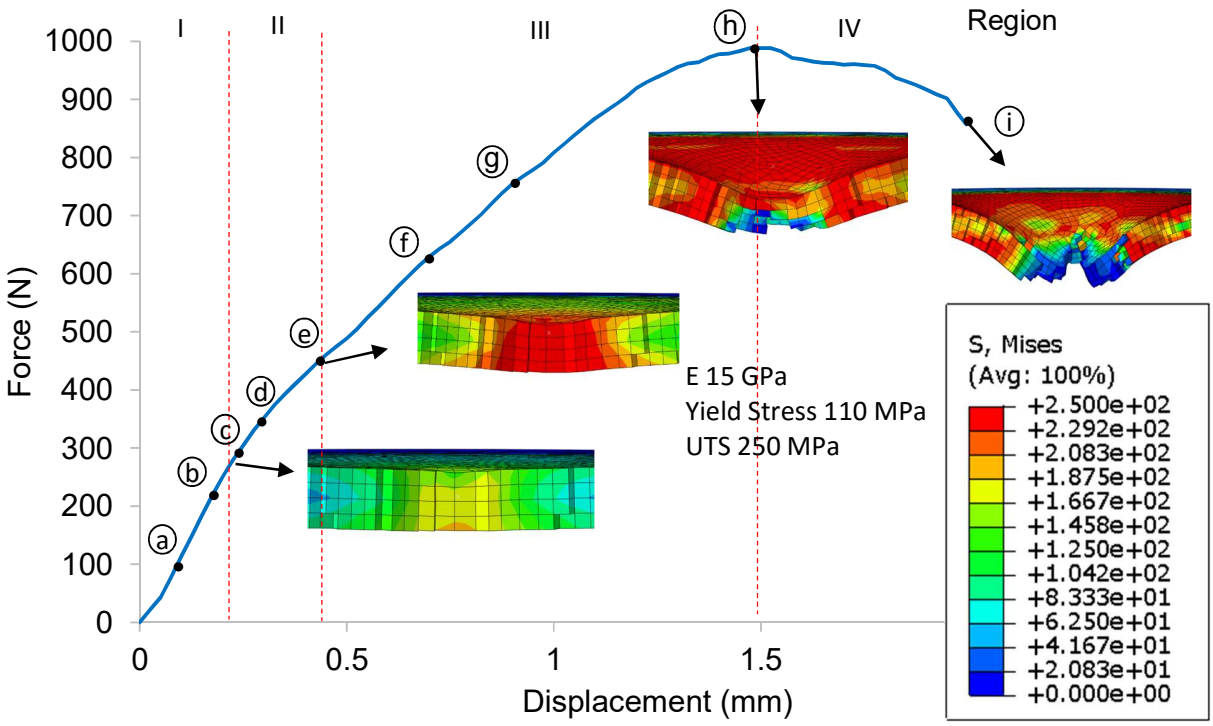

Figure 10. Locations selected to be analyzed on a typical force vs displacement curve

Before the loading reached region II, the local area experienced a yield-bending process. In region I, the stress of the elements on the top surface of the disc was larger than the stress on the bottom, as plotted in Figure 11.

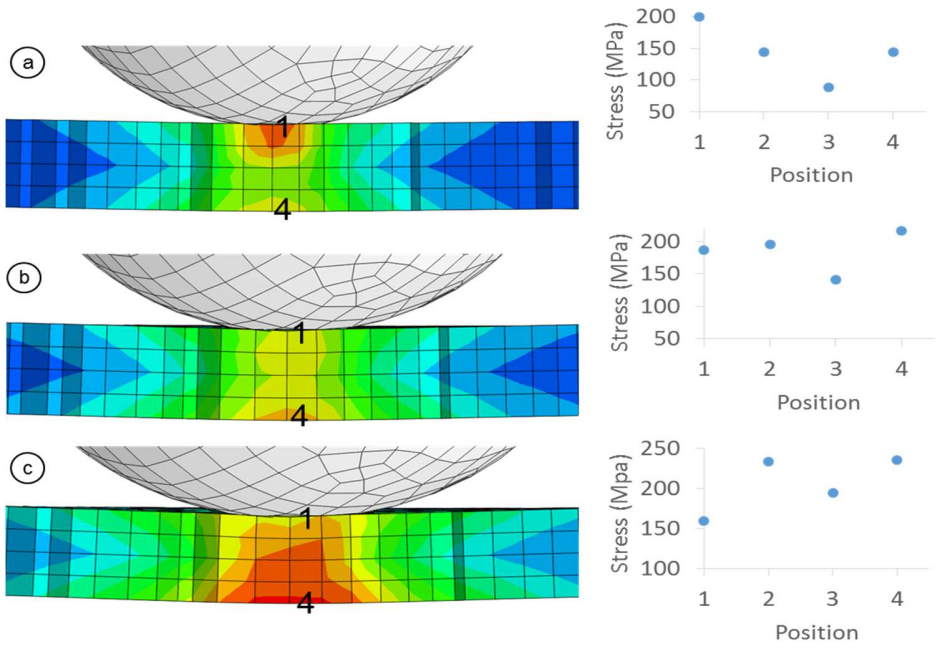

Figure 11. Stress distribution at different locations on the curve

The position vs stress distribution in Figure 11 refers to the element labeled in the cross-sectional view of the disc from top to bottom. The yield stress of the material was 110 MPa. As seen in in Figure 11, cross section (a), the stress of element 3 was still under the yield stress. As seen in cross section (b), when the disc was about to pass from region I to region II, all four elements had yielded. The force vs displacement curve also showed a different stiffness transition in this period. So this region is called *elastic bending*. This bending continued until the yield stress had spread throughout the thickness of the disc.

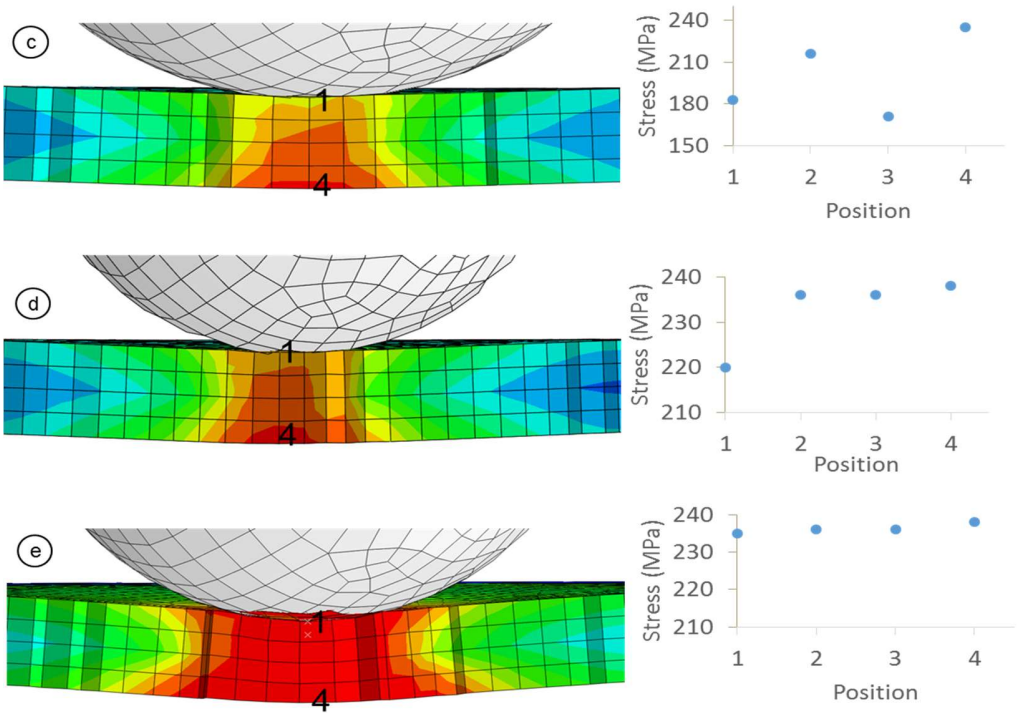

Figure 12. Region II – Plastic bending

Once the disc passed the yield force, plastic stress was produced, which caused strain hardening. As seen in Figure 12, the process was mainly dominated by the plastic properties of the material. Greater stress started to increase from position 4 until all the elements from bottom to the top at the center reached the ultimate strength of the material. Since the local central area undergoes plastic deformation, this region is called *plastic bending*.

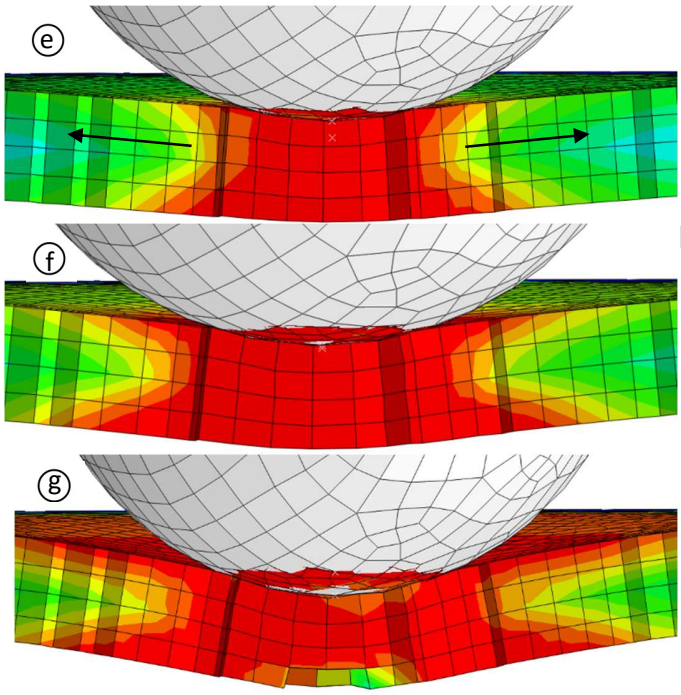

Figure 13. Region III – Membrane stretching

After elements in all four positions reached the ultimate stress, the ultimate stress distribution started to expand horizontally along the disc as the punch kept going downward. As the element kept deforming, void nucleation began to occur from the bottom of the disk. It led to crack propagation and the disc failed.

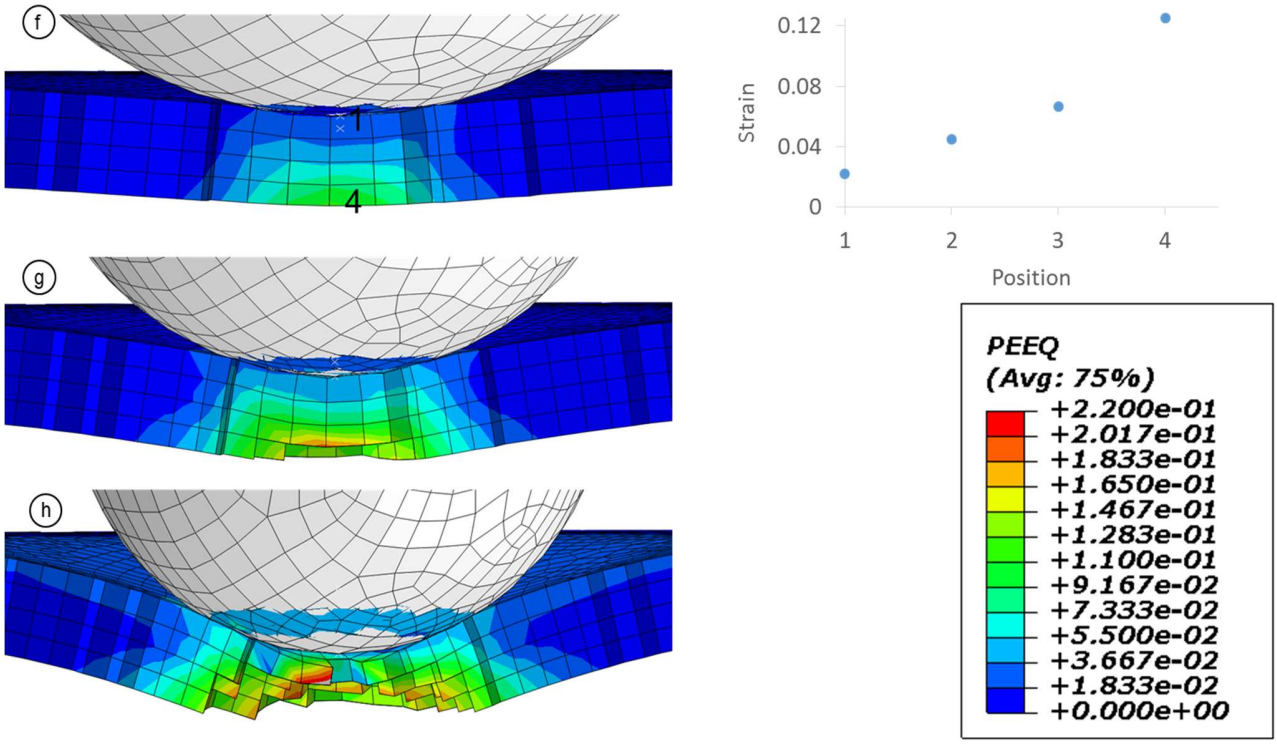

Figure 14. Strain distribution in region III – Membrane stretching

Strain distribution is shown in Figure 14, cross section (f). The damage setting in this model used strain-dependent criteria. The element was deleted when the plastic strain reached 0.22. This region exhibits the initiation of the failure and material degradation.

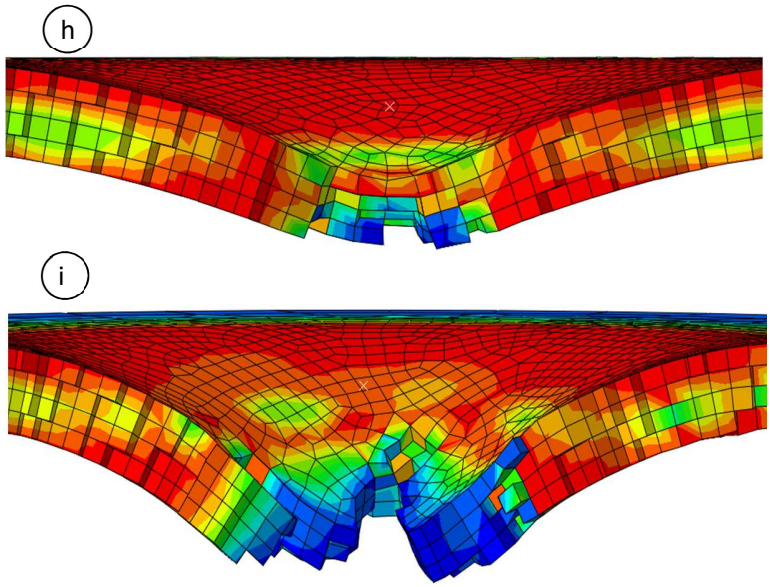

Figure 15. Region IV – Plastic instability

Finally, the disc was perforated and the load decreased as the crack was propagated in the last stage, as shown in Figure 15. Limited study was conducted in this region because damage behavior is generally unpredictable.

2.4.3 Effects of Material Properties on Force vs Displacement Curve

Many studies have established correlations between SPT results and material tensile properties [4, 5]. However, these correlations are often empirical since material behavior in the SPT is complicated and varies with different punch ball sizes, disc thickness, temperature, and die clearances [4, 5, 17]. In this subsection, the effects of material properties on the force vs displacement curve are studied.

Material property parameters of σ_y, σ_{ult}, ϵ_{fra}, and E were selected to be studied since these parameters dominate the curve trend in different regions. Table 2 shows the values of each parameter studied.

Table 2. Values of each parameter studied

Parameters	Value
Young's Modulus (GPa)	15*, 30, 40
Yield Stress (MPa)	50, 80, 110*
Ultimate Stress (MPa)	200, 250*, 300
Fracture Strain	0.14, 0.16*, 0.18

*The common values are the values marked with *.*

Figure 16 shows the effects of the SPT on the output of different material's Young's modulus. With a larger Young's modulus, the curve in region I was stiffer. These curves all have about the same slope after region I, which indicates that the Young's modulus of the material is the primary influence in region I.

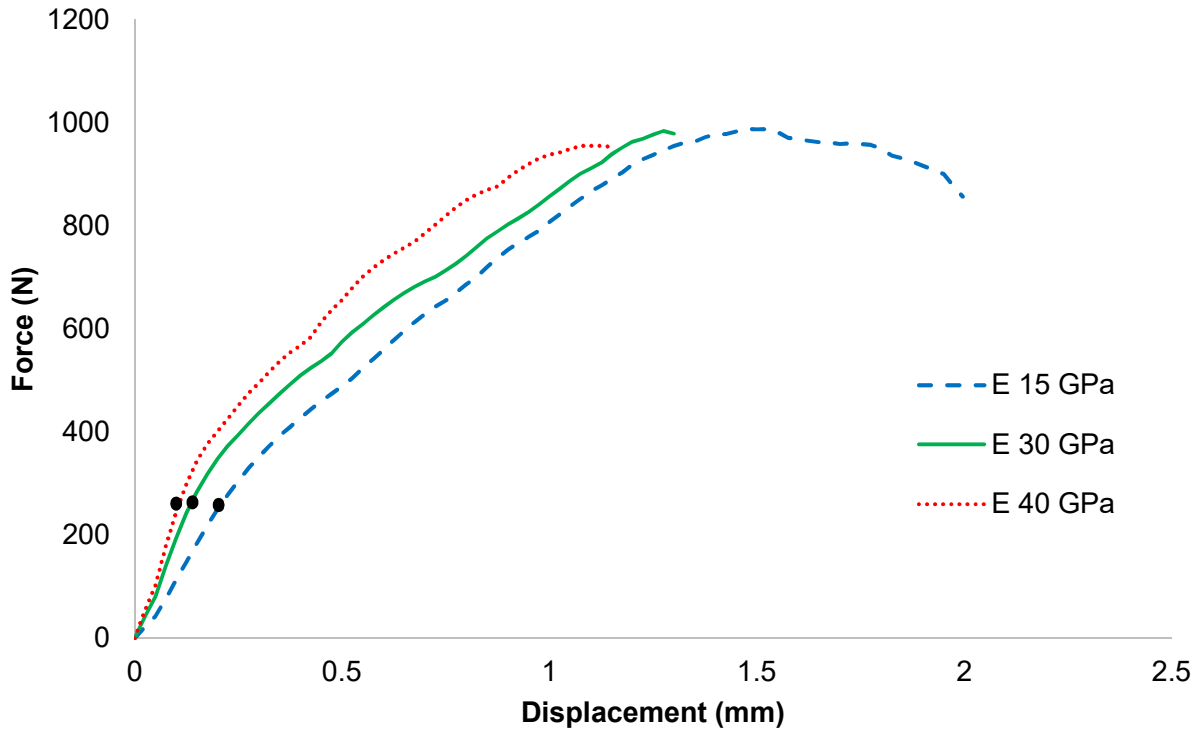

Figure 16. SPT models with three different Young's Modulus

The highlighted points shown in Figure 16 are listed in Table 3. All three points are within the region I. With a similar force response, the values of displacement were different, which indicates the Young's modulus effect.

Table 3. Output of highlighted points on the curve

Young's Modulus (GPa)	15	30	40
Displacement (mm)	0.18	0.12	0.09
Force (N)	235	243	240

Yield strength is related to yield load on the SPT curve. The yield load is the point of intersection of two tangential lines from regions I and II [4, 11]. Different material yield strengths caused the yield load to change only as shown in Figure 17.

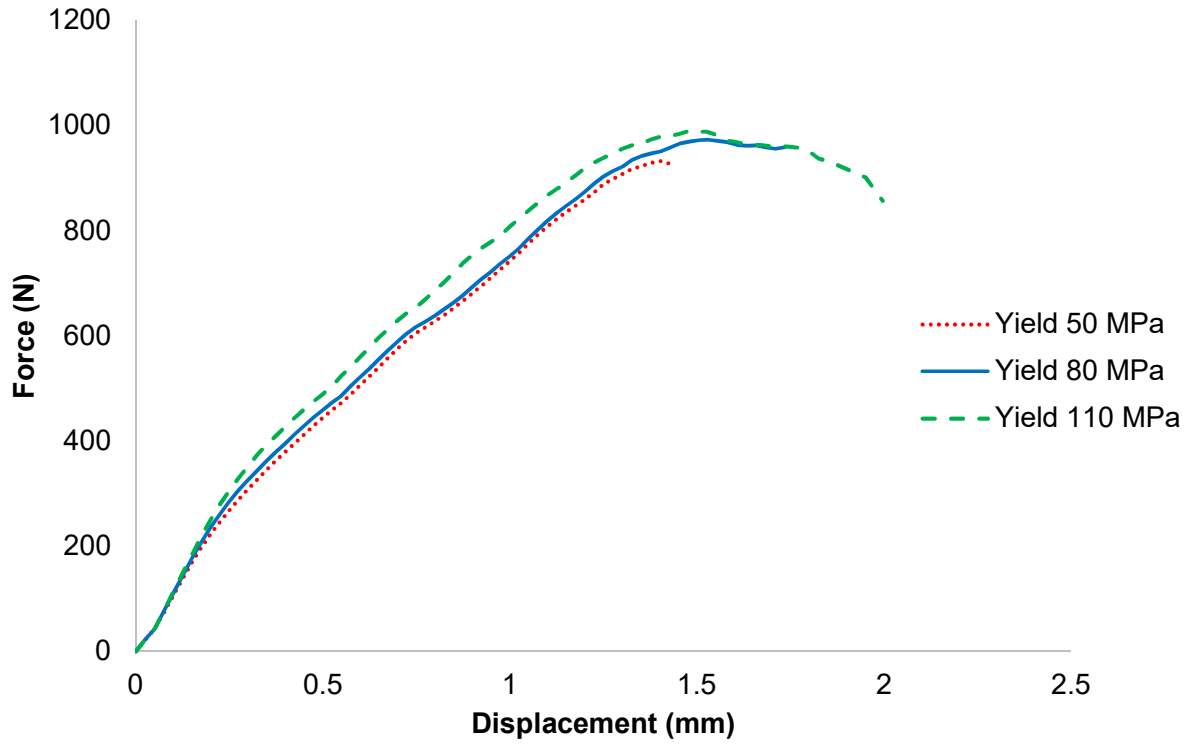

Figure 17. SPT models with three different yield strengths

A material's ultimate strength determines its plastic deformation in SPT, which starts in region II. In the simulation model of region II, elements at the bottom of the disc first started to bend with increased stress. The disc with greater ultimate strength had in a higher load response after region I. Figure 18 shows the effects of the ultimate strength of different materials on the SPT curve.

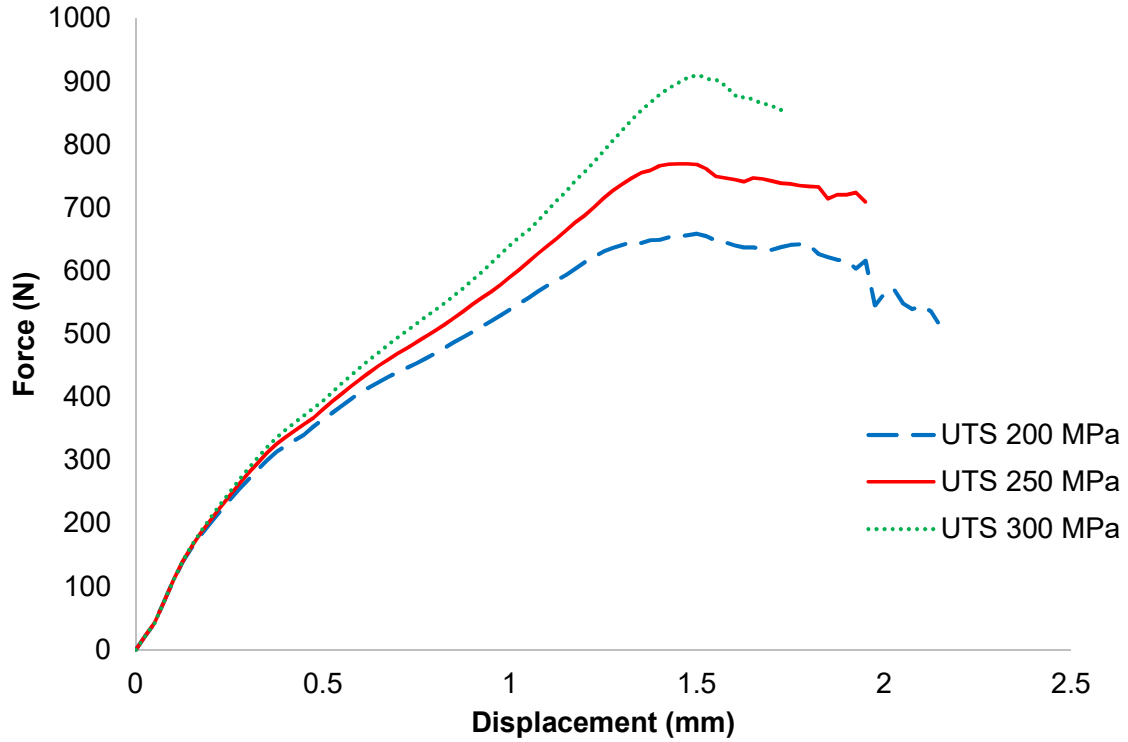

Figure 18. SPT models with three different ultimate strengths

Increasing the fracture strain of the material while keeping other material properties the same delayed the fracture in regions I and II and most of region III. As seen in Figure 19, the larger fracture strain caused the curve to have a larger maximum force with larger displacement compared with the other two. Table 4 shows the force and displacement value at the peak point on the curve.

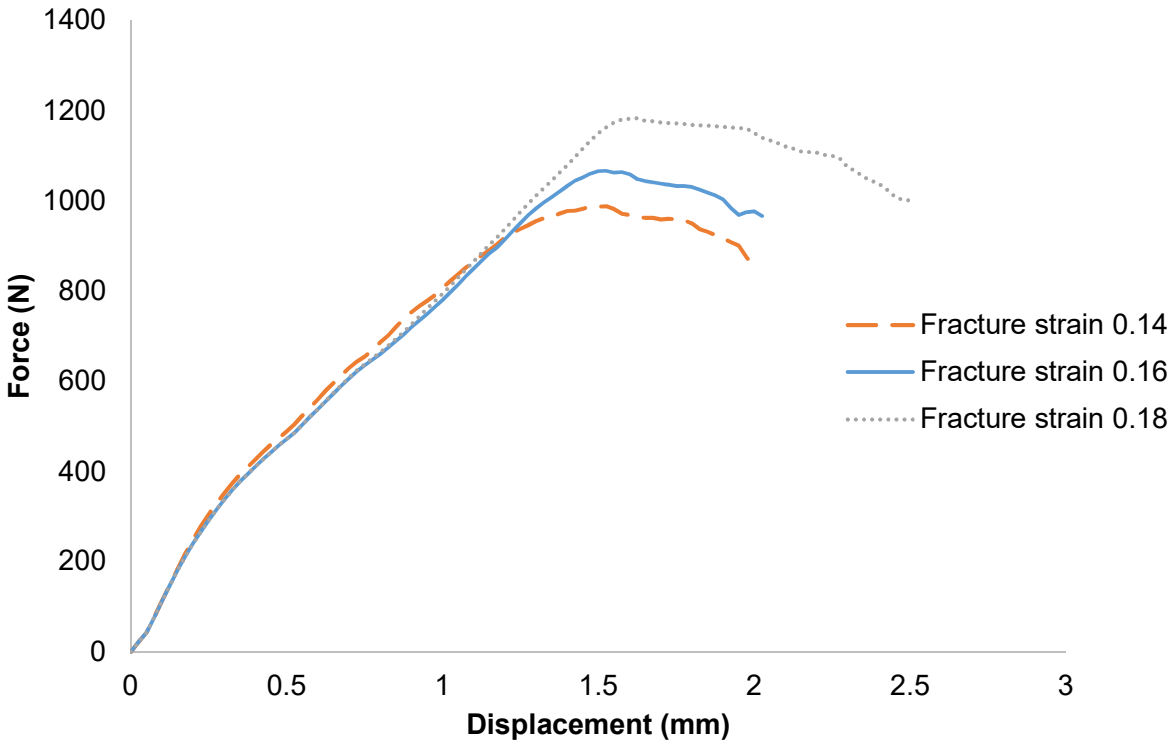

Figure 19. SPT models with three different fracture strains

Table 4. Force and displacement value at the peak point on the curve

Fracture Strain	0.14	0.16	0.18
Displacement (mm)	1.48	1.53	1.63
Force (N)	988	1066	1183

2.4.4 Energy Dissipation During the SPT

Lots of work has been done to correlate SPT results with material tensile properties [4-8]. However, the correlations have been limited to certain groups of metallic materials such as steel, copper, and aluminum. They have only been estimations [4]. In this section, the energy absorbed in tensile mode ($\sigma \cdot \varepsilon$) was compared with the SPT. The SPT was associated with multiple stages of the deformation process, including elastic yielding during the first stage and plastic

deformation in the following stages. The deformation process had a similar pattern to that of the tensile mode.

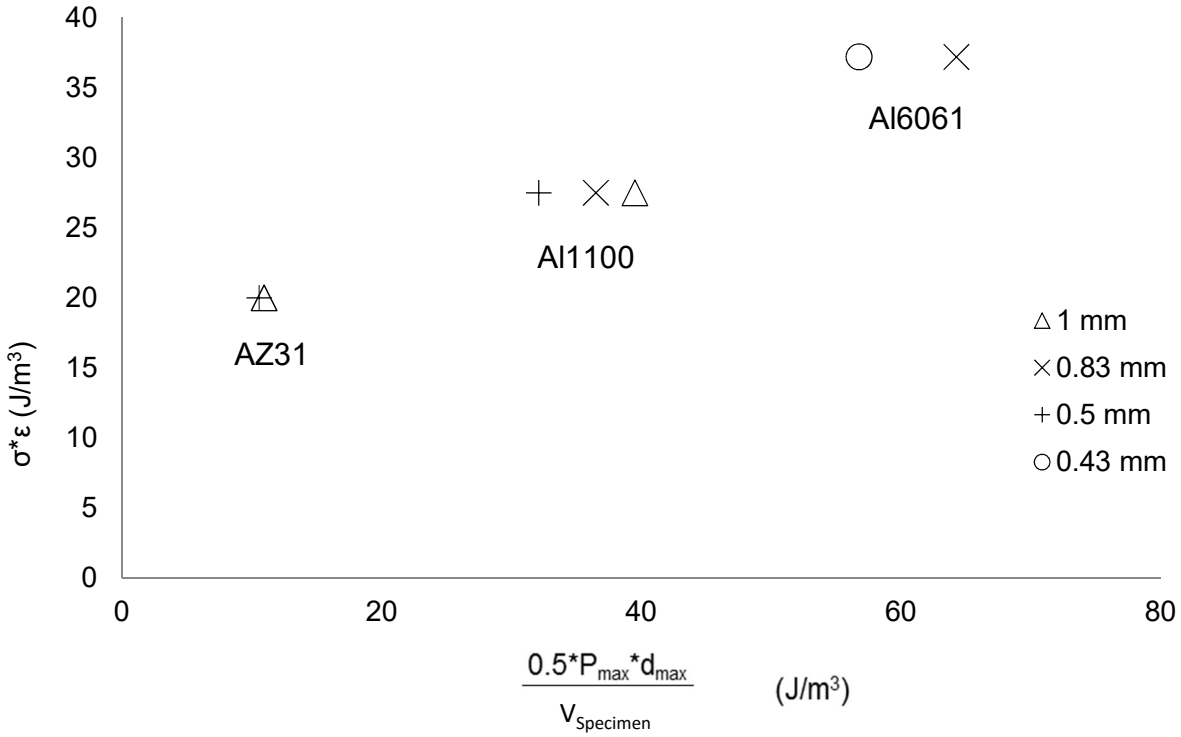

Figure 20. Energy consumed in the SPT vs. tensile mode with different thicknesses of different materials without thickness effects term

In Figure 20, materials with different thicknesses are illustrated on the graph for energy dissipation. The y-axis represents σ*ε, which is an estimation of energy dissipated per unit volume in tensile mode. The term is calculated by estimating the area of each material's tensile stress strain curve from the beginning to the fracture point. Table 5 lists the material tensile properties of Al1100, AZ31, and Al6061.

Table 5. Partial material properties of tested metal

Material	Al1100[18]	AZ31	Al6061[18]
Yield Strength (MPa)	35	110	276
UTS (MPa)	125	250	310
Elongation	0.22	0.08	0.12

In the x-axis, $0.5*P_{max}*d_{max}$ was the total energy consumed during the SPT. $V_{specimen}$ was the effective volume of the round disc that was tested. However, the data points corresponding to different thicknesses within the same material were scattered. This was mainly due to the effects of specimen size and the size of the punch ball. With a thinner disc and/or a smaller punch ball, the influence of localized stress was larger.

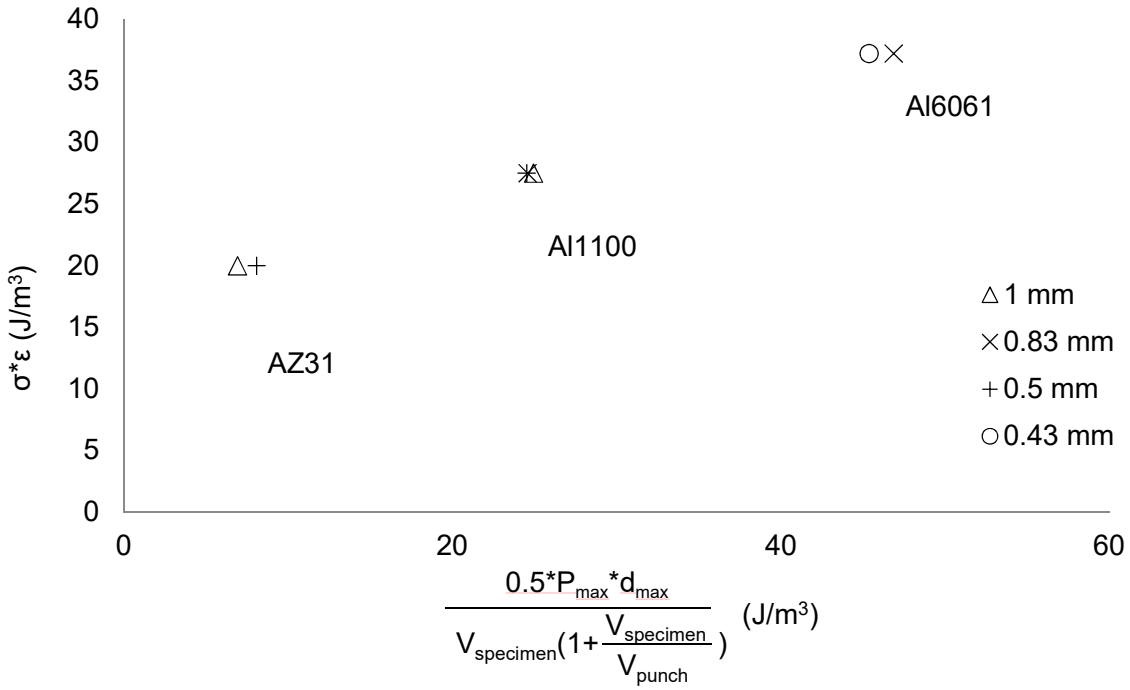

Figure 21. Energy consumed in the SPT vs tensile mode with different thicknesses of different materials

We propose that an additional term be used when calculating energy dissipation in the SPT as follows:

$$\frac{0.5 * P_{max} * d_{max}}{V_{specimen}(1 + \frac{V_{specimen}}{V_{punch}})} \quad [1]$$

This additional term accounts for the size of the punch ball in relation to the volume of the material absorbing the deformation. Figure 21 shows the replotted figure with the additional term proposed in Equation [1].

2.5 Conclusions

The main focus of this chapter has been to understand the SPT through numerical simulation. With simulation, the well-established four stages of the typical force vs displacement curve of the SPT—elastic bending, plastic bending, membrane stretching, and plastic instability—were analyzed. In the elastic bending stage, the specimen experienced an elastic deformation. The stage was mainly dominated by the material's elastic modulus properties. The plastic deformation and membrane stretching stages were affected by the material's isotropic hardening properties. The fracture strain of the material affected the last stage, plastic instability. Material with a larger fracture strain had a larger displacement and a larger maximum force. Finally, we proposed a modified energy dissipation equation for the SPT after comparing it with energy dissipation in tensile testing. The modified equation removed the influence of specimen thickness and relative ball size.

CHAPTER 3. SIMLUATION OF THE SMALL PUNCH TEST ON A PATTERN-REINFORCED LAMINATED COMPOSITE

3.1 Introduction

Metal matrix composite has always been a promising type of material. Conventional fabrication approaches for metal composites include stir casting [18-23], powder metallurgy [24-26], and squeeze casting [27, 28]. The number of metal matrix composites has also increased in in the past decade, comprising layered composites, nanoscale composites, and bio-derived composites [29]. Recently, Bastwros and Kim [30]developed a fabrication technique using ultrasonic spray with Al sheets and SiC particles to create complex laminate composite structures made of metal composite materials.

Magnesium alloy has been widely employed and studied in the automobile and aerospace fields because of its light weight, high stiffness, high specific strength, and good machinability [31]. It is also a good candidate for use as a matrix material in composite materials. Another experiment was carried out by Bastwros using AZ31 sheets and SiC particles as reinforcement material. The SPT was used to prove that such complex laminate structures enhance material strength.

Simulation tools have been utilized during the SPT to analyze and understand the deformation behavior of pattern-reinforced laminated composites. Researchers have done a lot of work using FEA for laminate composites. Most of the time, FEA was used to analyze delamination and transverse shear cracks in these composites [32]. Flatscher used simulation to explore the intralaminar plasticity, damage, softening, and open-hole failure mechanism [33]. Zhao analyzed the delamination of unidirectional and multidirectional laminates with FEA

simulation [34]. But we have found no study related to such complex laminate structures. In this work, a three-dimensional FEA model was developed for composite materials and simulated using the SPT FEA model.

3.2 FEA Model and Experimental Procedures

The aim of this section is to verify the Al/SiC composite layer/pattern tensile property by comparing the results of the experiment with the FEA model. The Al/SiC composite material properties are first estimated as a range using the rule of mixtures. Then they are verified by comparing the results with the experiments. The actual composite specimen is made using a spray-assisted, semisolid compaction manufacturing process. The specimen in FEA is modeled to mimic the actual composite specimen fabricated. The FEA model for the SPT setup is the same as the one introduced in Chapter 2.

3.2.1 Experimental Procedure

The specimen was made by consolidating 14 layers of AZ31 that had been sprayed with Al6061 and SiC particles. Each layer was 74 μm thick. Figure 22 shows the ultrasonic spray system used for spraying the particles.

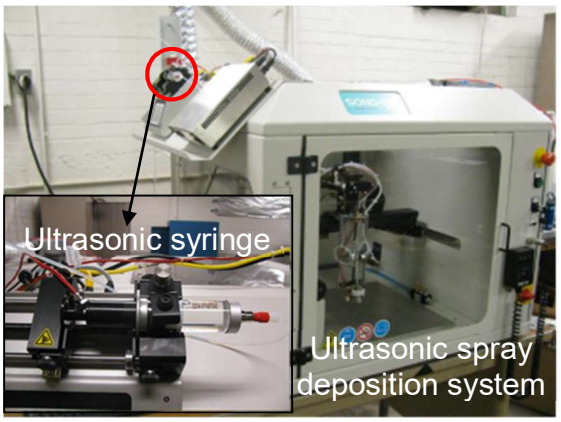

Figure 22. Ultrasonic spray deposition system

The nanoparticle suspension contained 0.05 wt.% SiC nanoparticles (80 nm) and 0.015 wt.% Al6061 particles (1.73 µm). The sprayed surface was heated up to 300°C to evaporate the suspension liquid while spraying. The sprayed layer was mixed at a volume ratio of 2:3 for Al6061 and SiC particles. The mixture was sprayed onto the AZ31 foil discs in two configurations. One was a uniformly sprayed layer on the surface of the AZ31 discs. The other was sprayed in a circular configuration 800 µm in diameter using a mask pattern during the spraying, as shown in Figure 23.

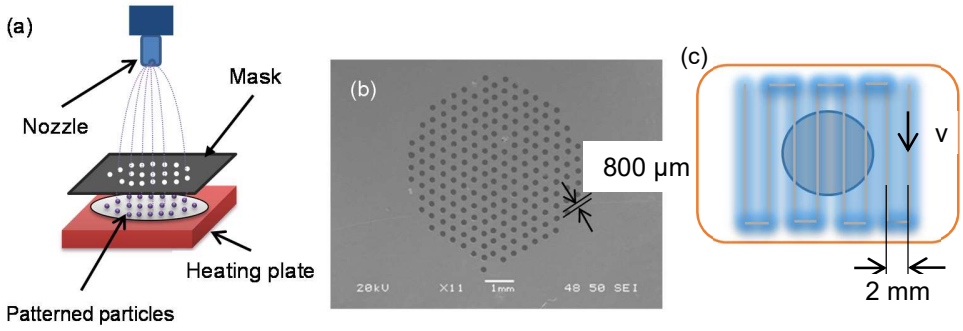

Figure 23. Spray procedure setups (a) overall setup, (b) mask, (c) spray path

The assembled layers were first pre-compacted at 100 MPa. The sheets were heated up to 610ºC with a pressure of 50 MPa for 20 min. The liquid phase percentage at this temperature was approximately 9%. The furnace is shown in Figure 24.

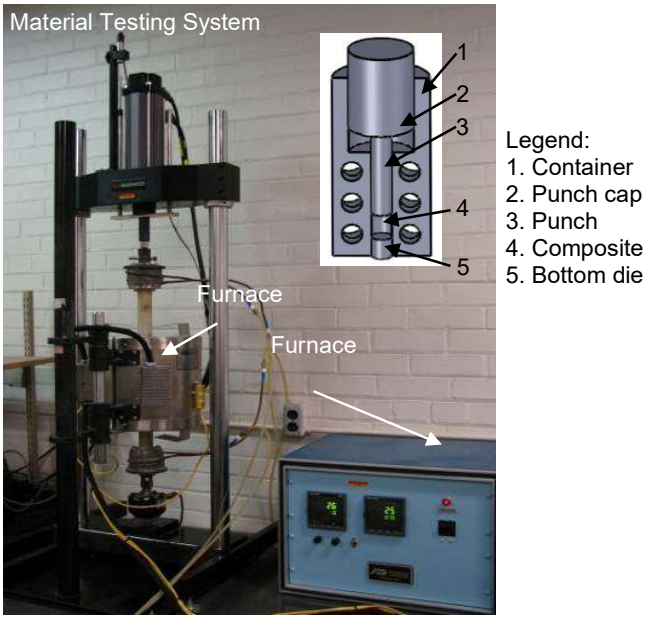

Figure 24. Furnace used for consolidating the sheets

3.2.2 FEA Model

To mimic the structure of the composite specimen, 27 layers were modeled and a tie constraint was used. There were 14 layers of AZ31 with a thickness of 74 μm and 13 layers of the uniformly sprayed composite layer with a thickness of 2 μm. The model used was a full-scale 3D model for pattern-reinforced composites and a 2D quarter model for uniformly sprayed alternating composites, as shown in Figure 25. Figure 26 shows the schematic of the pattern layer.

- 2D model

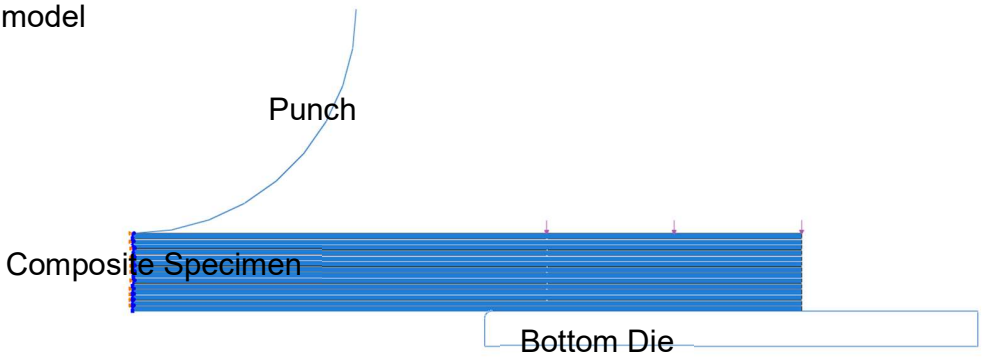

- 3D model

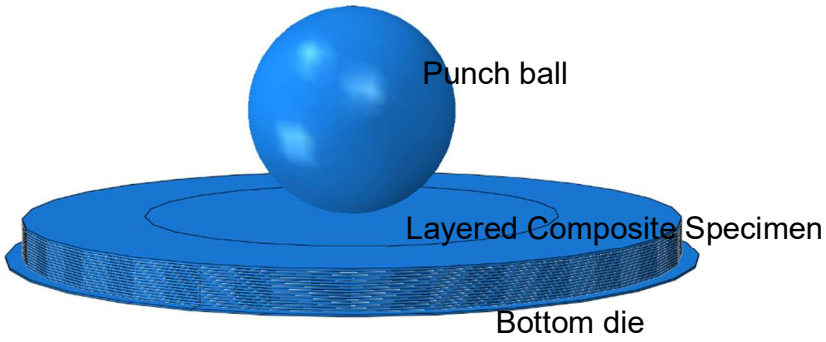

Figure 25. Schematic of the FEA model

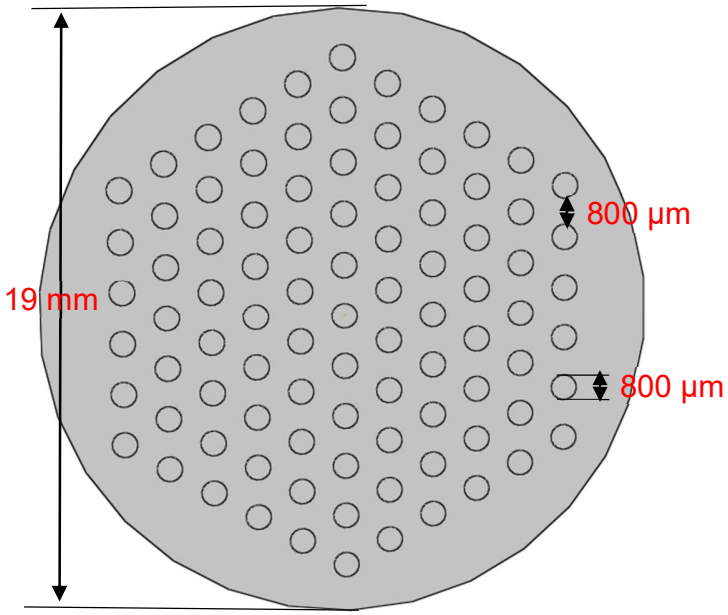

Figure 26. Schematic of the pattern layer

During the hot compaction, the AZ31 reached a semi-solid state where the solid and liquid phases coexisted. The soft and low viscosity of the liquid allowed it to fill in the porosity between the particles. The rule of mixtures was used to estimate the material properties of the composite layer, as listed in Table 6.

Table 6. Material properties of SiC, AZ31 and Al6061

Material Property	SiC	AZ31	Al6061
Poisson Ratio	0.14-0.192	0.33	0.33
Young's Modulus (GPa)	410	8.5	69
Yield Strength (MPa)	525	110	276
UTS (MPa)	525	250	310

The rule of mixture predicts both the upper and lower bounds of the composite material properties. The upper bound of the material property is predicted by:

$$M_{upper} = f_{SiC}M_{SiC} + f_{AZ31}M_{AZ31} + f_{Al6061}M_{Al6061} \quad [2]$$

The lower bound is established by:

$$M_{lower} = \left(\frac{f_{SiC}}{M_{SiC}} + \frac{f_{AZ31}}{M_{AZ31}} + \frac{f_{Al6061}}{M_{Al6061}}\right)^{-1} \quad [3]$$

where f is the volume fraction of the reinforcement phase, M is the material property parameter, which could be the Poisson ratio, Young's modulus, yield strength, UTS, or density.

The weight ratio of SiC to Al6061 was about 3:2. The volume ratio was calculated as 1:0.6. The volume ratio between Mg and SiC was about 2:1 based on the EDS scan data, as shown in Figure 27.

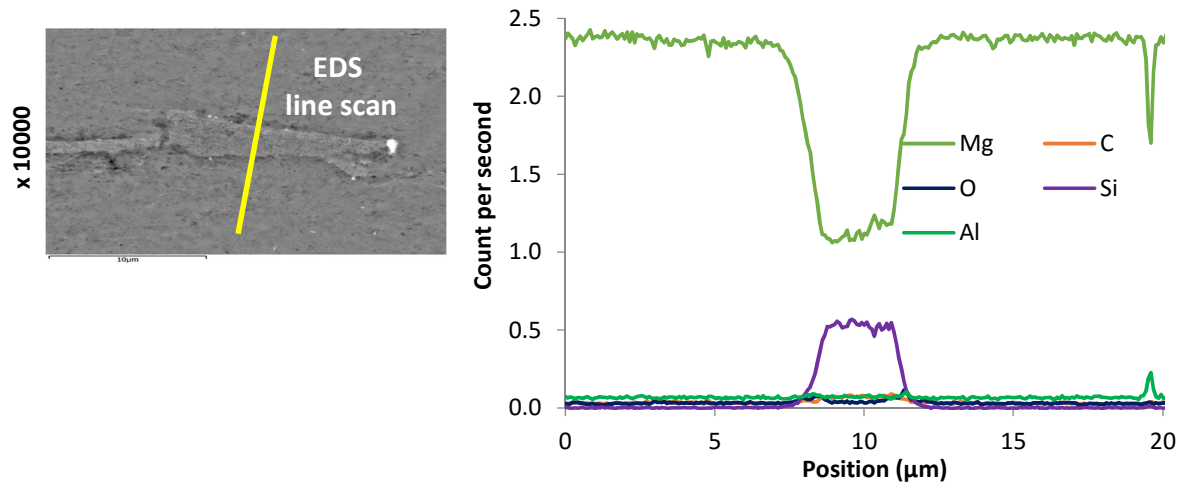

Figure 27. EDS line scan across the interface between two AZ31 foils, and elemental diffraction intensity along the line scan with respect to the position on the scanned line

As a result, the volume ratio of the three materials was 2:1:0.6 for AZ31, SiC, and Al, respectively. So the volume fractions used for calculation were 54%, 19%, and 27% for f_{AZ31},

f_{Al6061}, and f_{SiC}. The volume percentage presents the fraction of the Al/SiC composite material. AZ31 is included in the composite material because the AZ31 sheets fill in the porosity between the SiC/Al particles during the hot compaction process. So it has to be counted when estimating the properties of the composite material. The upper and lower bounds were calculated and are presented in Table 7. The final material properties were verified by comparing the FEA model with the experimental results. The force vs displacement curve is shown in Figure 28. The simulation results showed good agreement with the experiments.

Table 7. Composite material property estimation using rule of mixtures

Material Property	Upper Bound	Lower Bound	Verified
Poisson Ratio	0.29	0.25	0.268
Young's Modulus (GPa)	126	21	69
Yield Strength (MPa)	264	188	223
UTS (MPa)	334	308	320

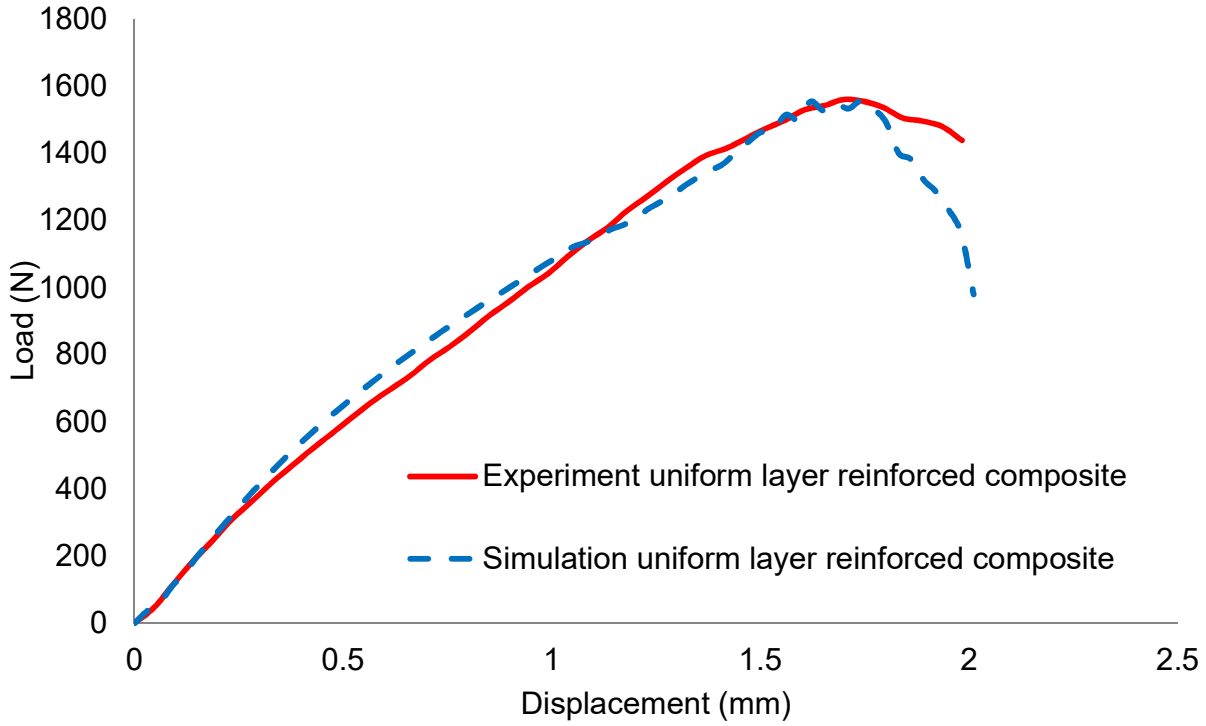

Figure 28. Force vs. displacement curve from the experiment and simulation of the uniform spayed layer composite

3.3 Simulation of Pattern-Reinforced Composite

The experiment showed that with the same amount of loading of the SiC and Al6061 particles, the pattern-reinforced composite showed higher strength than the uniformly sprayed composite. A uniformly reinforced composite model was made to compare with an 800 µm circular pattern-reinforced composite. Both of them had a loading percent of 0.06% wt. The composite layer of the uniformly reinforced model had a layer thickness of 0.4 µm. The actual sprayed pattern size is shown in Figure 29 in a photograph taken by a scanning electron microscope (SEM).

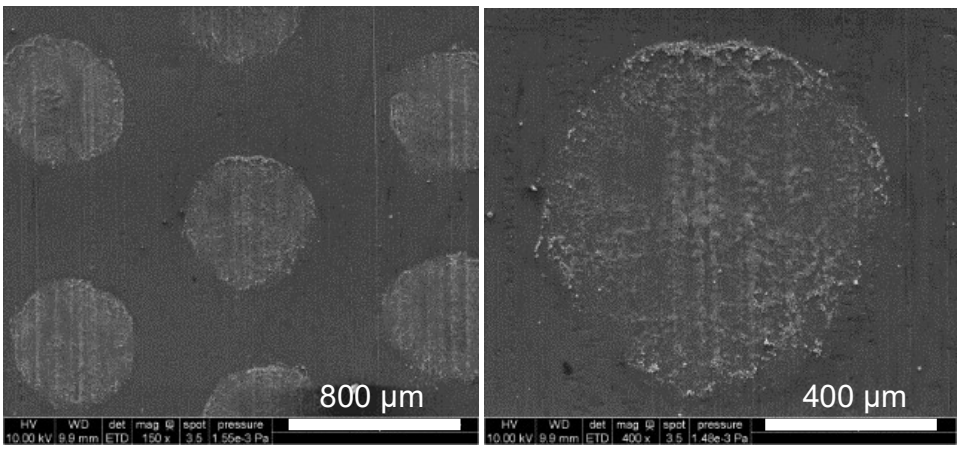

Figure 29. Actual sprayed pattern on AZ31

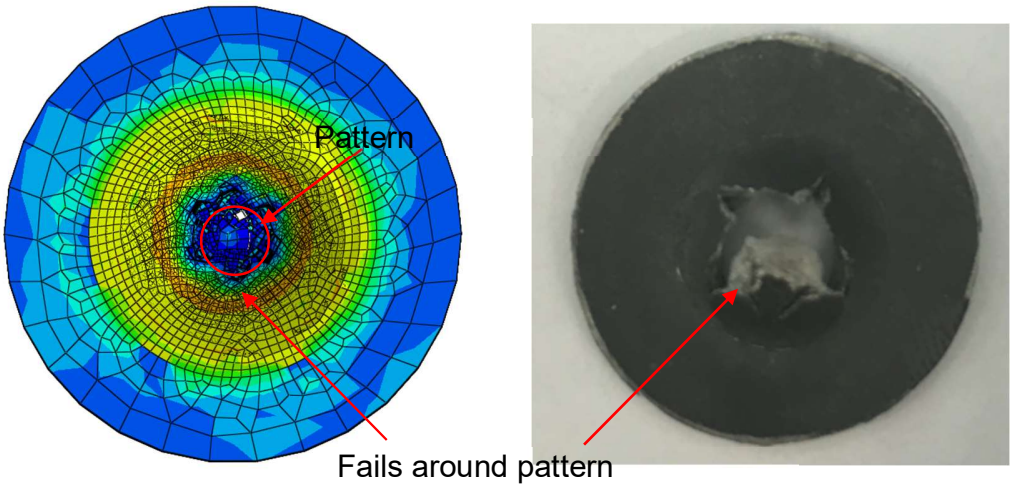

Figure 30. Failure comparison between simulation and experiment for the 2 µm sample

Figure 30 presents the fracture comparison between the FEA simulation and the experiment. Both results show that the hard phase in the composite holds its shape and resists bending. Unlike the uniform layer-reinforced composite, the fracture in the pattern-reinforced composite in both the simulation and the experiment occurred in the matrix material. This means that the matrix phase of the pattern-reinforced composite contributes to the deformation during the SPT when compared to the uniform layer-reinforced composite.

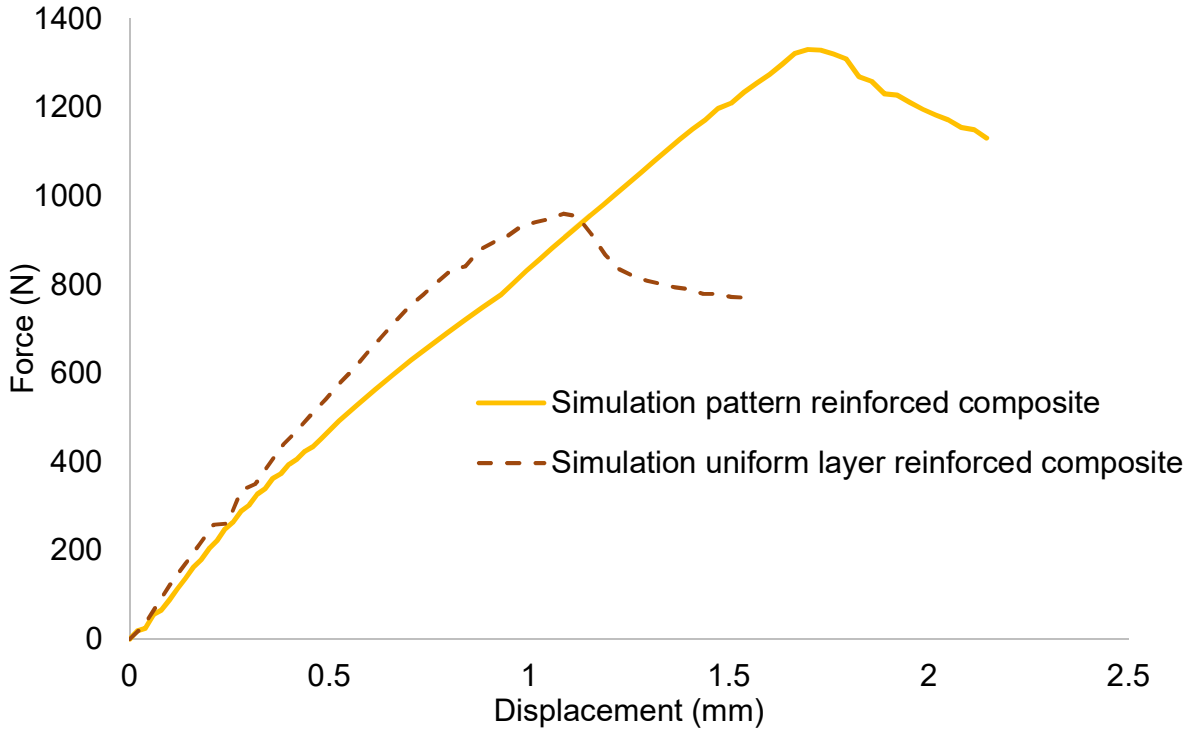

Figure 31. Force vs. displacement curve of the uniform reinforced layer composite and the pattern-reinforced composite following the SPT

As shown in Figure 31, the pattern-reinforced composite had greater strength and toughness. The uniform reinforcement increased the stiffness of the material because of the brittle composite layers. These brittle layers failed first and created cracks inside the specimen during the SPT. The stress and strain at selected locations of the two models were compared in order to study how the two reinforcement structures affected material strength. Ten elements were selected from the last reinforcement layer of each model. The 10 elements were chosen starting from the center of the layer and moving to the edge, as shown in Figure 32. The distance between all adjacent points was equal. In the pattern-reinforced layer, the elements were chosen from the hard phase and the matrix alternately starting from the single pattern at the center.

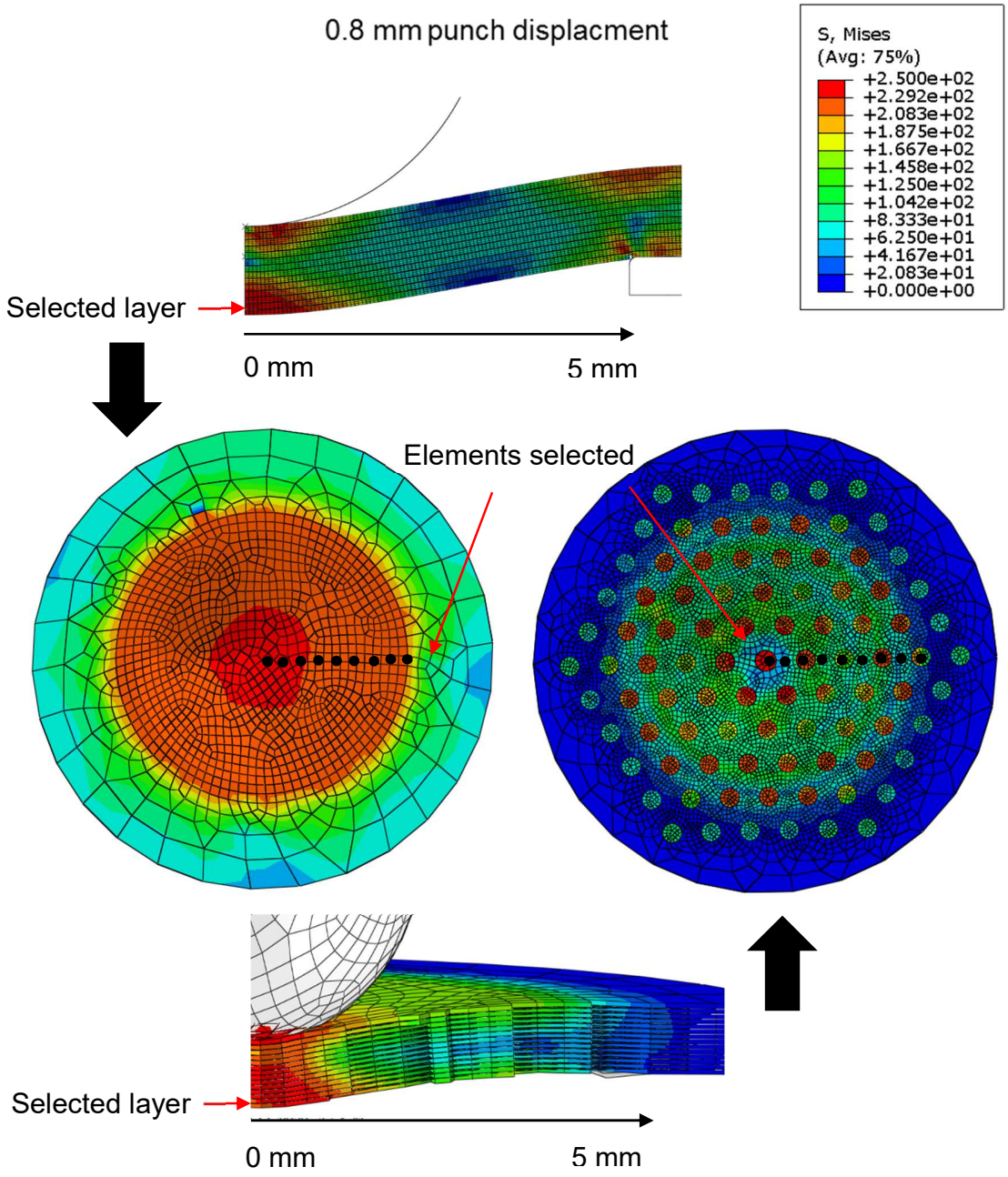

Figure 32. 10 Elements selected from the last layer of reinforcement

Von Mises stress and the equivalent plastic strain of these ten elements are plotted in Figure 33 and Figure 34.

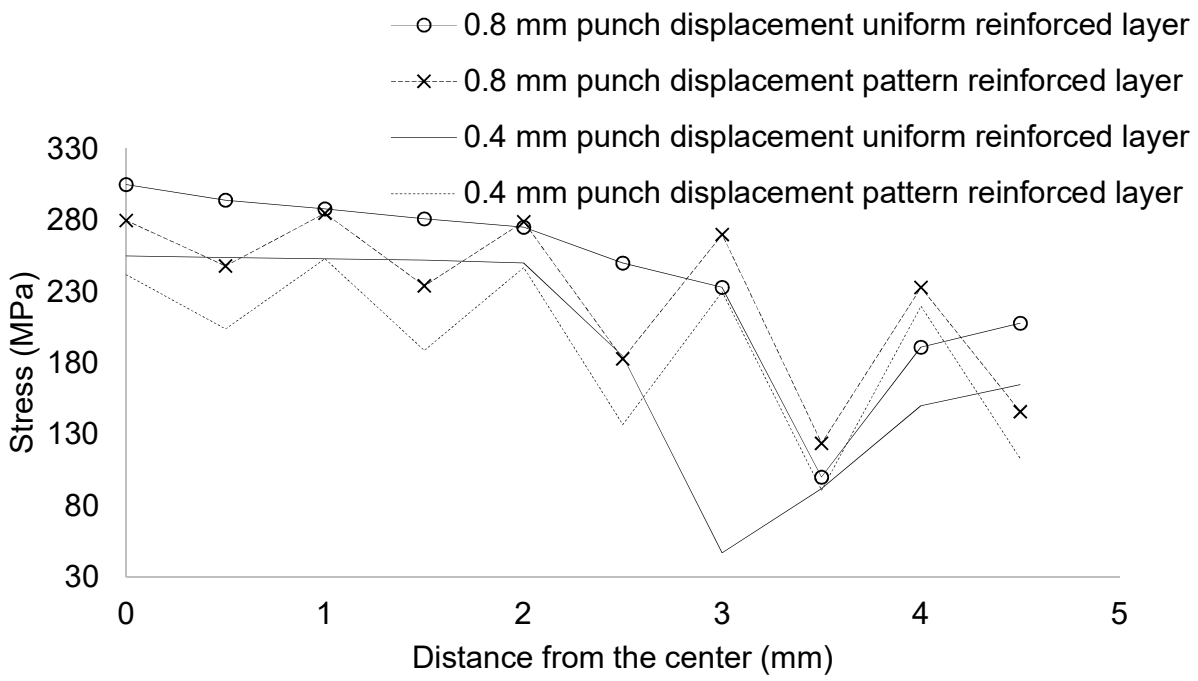

Figure 33. Stress comparison between uniform reinforced layer composite and pattern reinforced composite

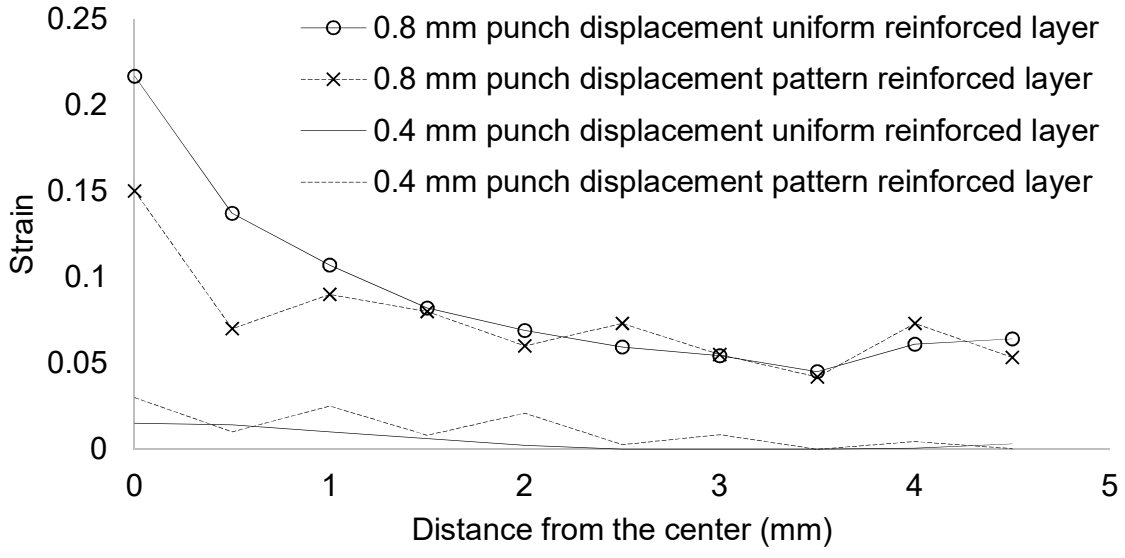

Figure 34. Strain comparison between uniform reinforced layer composite and pattern reinforced composite

As shown in Figure 33, larger stress was observed at 0 mm and 0.5 mm away from the center in the uniform reinforced composite. This indicates that a large localized stress was created at the center of the uniform reinforcement layer compared with the pattern-reinforced layer. In the uniform reinforced composite, the hard phase layer prevented most of the load from bending. This resulted in a high load concentration at the center of the thin and brittle reinforcement layer, which caused the layer to crack easily. In Figure 34, the plastic strain clearly shows that the center of the layer had a larger deformation at a punch displacement of 0.8 mm. But the pattern-reinforced composite had smaller localized stress and the hard phase patterns tended to share the load evenly. At a punch displacement of 0.4 mm, both composites showed a similar distribution of stress and strain. At a 0.4 mm displacement, the material was starting to transition from region I to region II. After the 0.4 mm punch displacement, the pattern-reinforced composite specimen moved into stage II, where the center of the disc was completely deformed. Then the material went through membrane stretching, constituting stage III. In contrast, the uniform composite specimen failed at stage II, the plastic bending stage. The plastic deformation did not occur through the entire thickness at the center of the specimen. This happened due to the uniform hard phase layers. The layers were non-ductile compared to layers in the matrix material. They resisted bending and failed at a smaller punch displacement. This created cracks that opened earlier than cracks in the pattern reinforced composite. A visual comparison is shown in Figure 32. The stress-strain comparison of the hard phase is presented in Figure 35 and Figure 36. The elements were selected from the center of the hard phase layer.

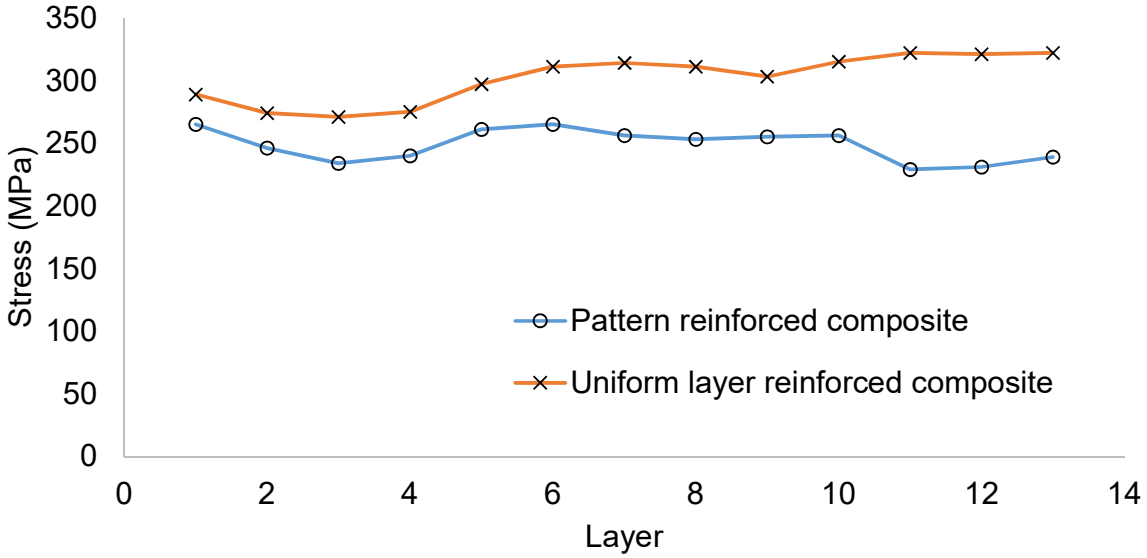

Figure 35. Stress in center of hard phase layer comparison between uniform reinforced layer composite and pattern reinforced composite through the thickness at 0.8 mm punch displacement

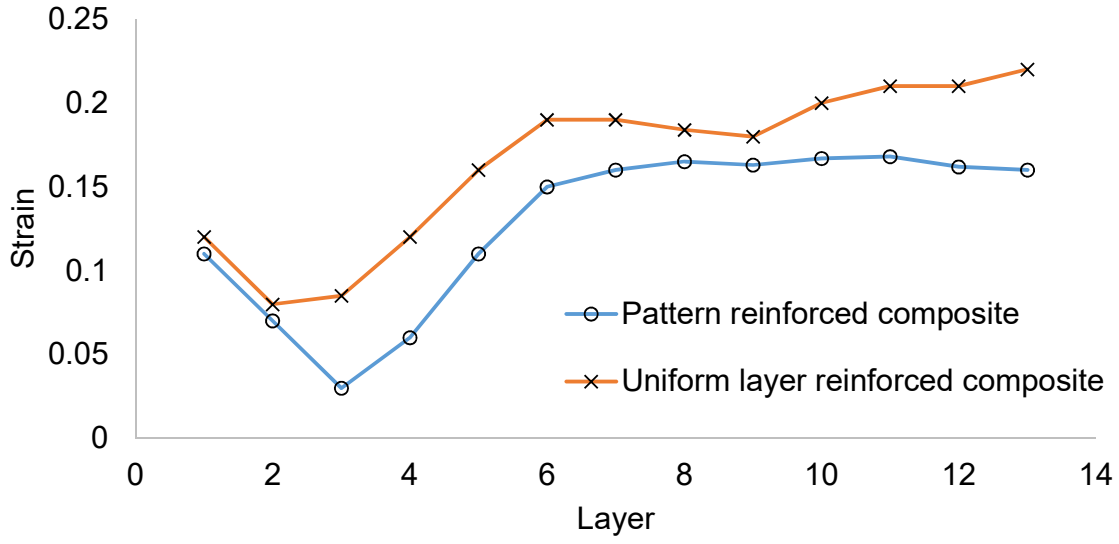

Figure 36. Strain in center of hard phase layer comparison between uniform reinforced layer composite and pattern reinforced composite through the thickness at 0.8 mm punch displacement

As shown in Figure 35, the hard phase material in the uniform layer-reinforced composite showed larger stress than the hard phase in the pattern-reinforced composite. This indicates that large localized stress in the center of the hard phase layer was produced. This large concentrated stress is dangerous and can cause a crack to open in the hard phase layer. As seen in Figure 36, greater strain was found in the hard phase layers of the uniform-reinforced composite, as expected. Within the uniform-reinforced composite, the larger strain occurred in layers close to the bottom. This indicates that the fracture started in the bottom layer of the hard phase. Once the crack began, the whole specimen soon failed.

3.4 Improved Design Analysis by FEA

The thickness of the reinforcement phase was increased to understand its impact on overall composite strength and ductility. Two additional pattern configurations of 20 μm and 50 μm in thickness were simulated, as shown in Figure 37.

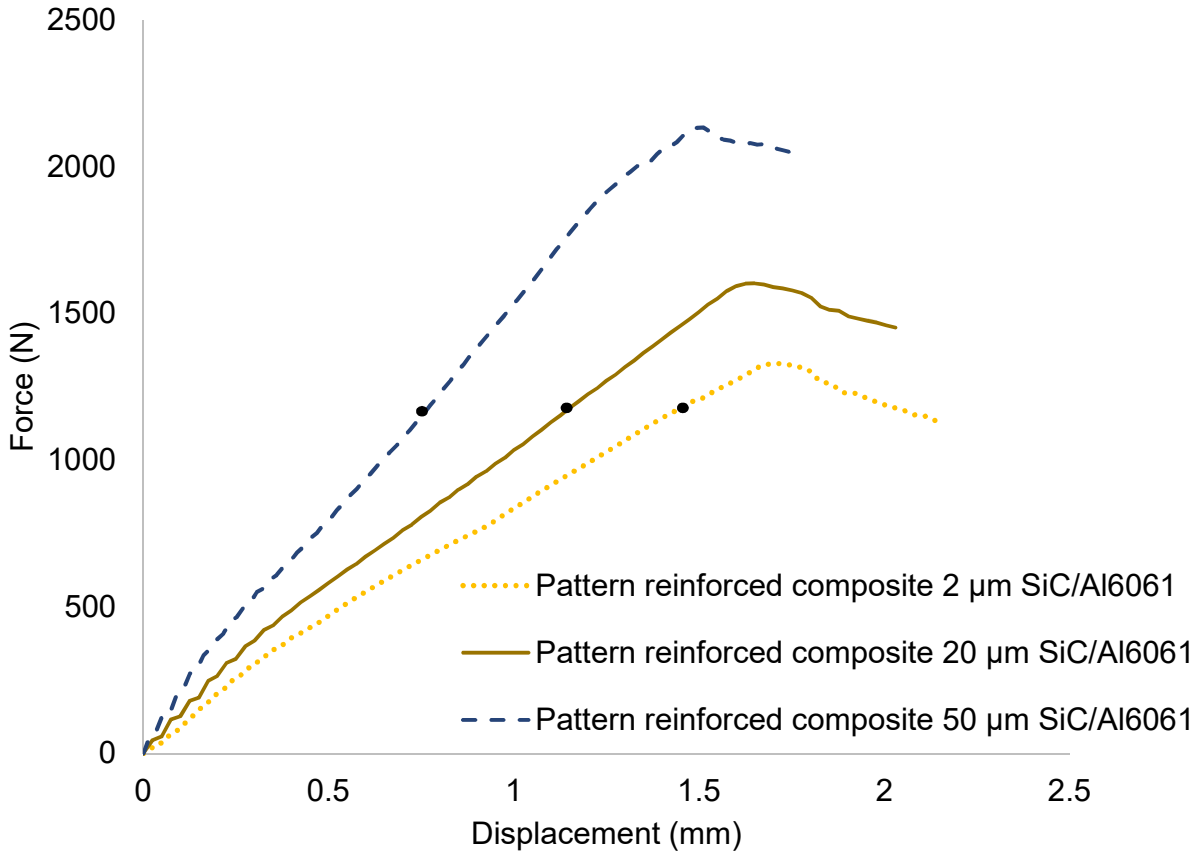

Figure 37. Simulation results for pattern composite with different pattern thicknesses

As shown in Figure 37, the strength of the composite material was enhanced as expected. The maximum load increased 60% with the 50 μm thickness pattern and 20% for 20 μm pattern. The maximum displacement decreased due to the larger amount of brittle phase material added to the composite. It reduced the overall ductility of the composite. The simulation results showed that failure always occurs in the matrix. But the hard phase did not fail in any of the three models.

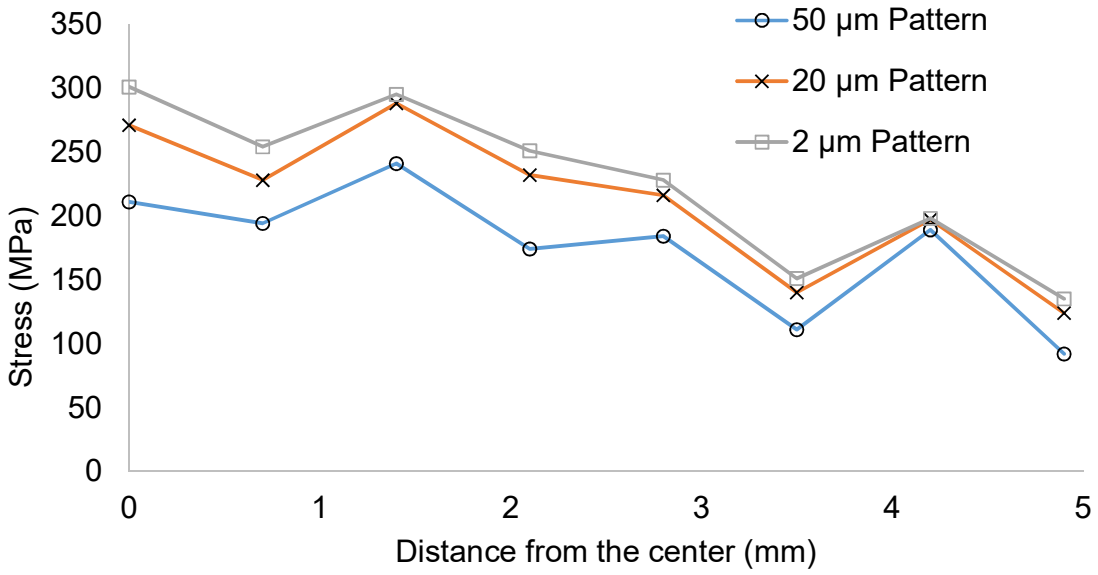

Figure 38. Stress comparison between different pattern thicknesses at force 1100 N

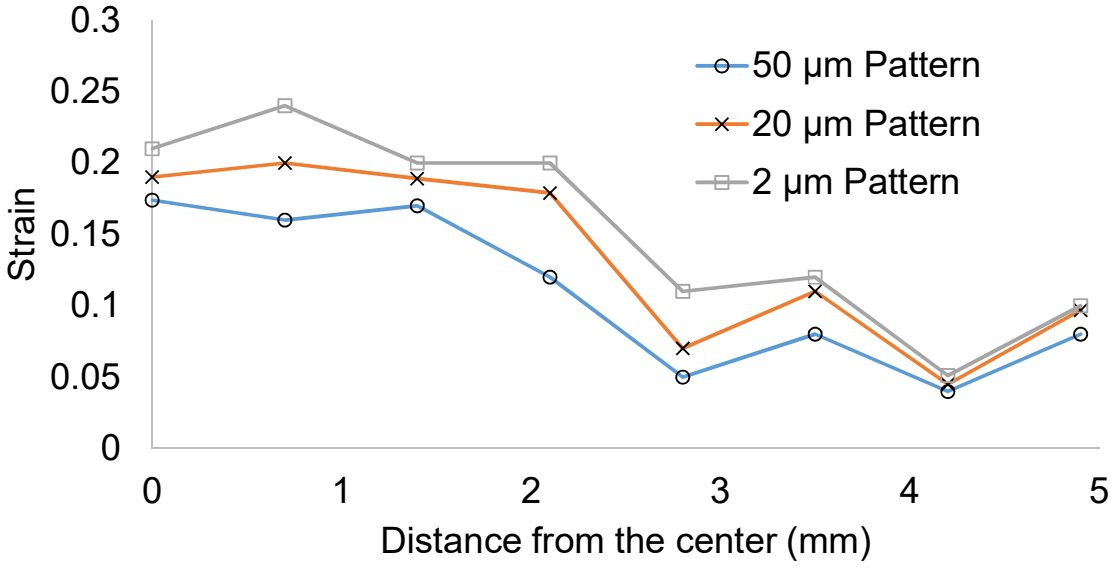

Figure 39. Strain comparison between different pattern thicknesses at force 1100 N

The elements in Figure 38 and Figure 39 were alternately selected from the pattern and the matrix starting with the pattern in the bottom pattern layer, as shown in Figure 32. Three models are compared at the same force response in the curve shown in Figure 37. The stress distribution of the thinner pattern composite is larger than the stress distribution in the other two models. More energy has dissipated in thinner pattern composite since it has a larger displacement at the same force response. Figure 39 shows that smaller thickness composite has a larger strain at the same force level. It indicates that the material is going to fail earlier than the material in the other two models.

3.5 Conclusions

Simulation was completed for the alternating uniform layer-reinforced composite and pattern-reinforced composite to understand the strengthening effects of the latter. In the uniform layer, highly localized stress was observed at the center of the composite during bending because the hard phase is unable to undergo deformation. This resulted in earlier cracks in the layer and the whole specimen failing at small deformations. The membrane stretching stage was absent from this composite because of the low ductility of the layer. With pattern configuration, the stress distribution was more uniform throughout each composite pattern. These patterns helped to prevent bending while the matrix material allowed deformation during stage III of the SPT, which led to better performance in material strength and ductility. With an understanding of the failure mechanism in the pattern composite, two thicker pattern reinforcement configurations of 20 μm and 50 μm pattern thickness were simulated. Compared with the original composite, the strength of the two thicker composites improved by 20% and 60%, respectively.

CHAPTER 4. SUMMARY

In this study, the strengthening effects of a pattern-reinforced composite were investigated using an FEA simulation method. The SPT was performed on a fabricated composite and the results were used to verify the FE model, which was then used for analysis. First, FEA simulation was used to investigate the influence of material properties, elastic modulus, yield strength, ultimate strength, and fracture strain on the four stages of the SPT. In addition, a modified energy dissipation equation was proposed for the SPT to eliminate the effects of sheet thickness and ball size.

The FE simulation was performed on pattern-reinforced composites, showing that the pattern reinforcement helped to distribute stress and strain during deformation. This resulted in higher strength when compared with a uniform alternating composite. A simulation tool was used to predict improved strengthening effects for thicker reinforcement phase designs of 20 μm and 50 μm.

The work showed that composites with complex structures may offer important properties that cannot be achieved using conventional composite systems. Further work is needed to accurately predict and understand the complex interactions between the different phases.

CHAPTER 5. BIBLIOGRAPHY

[1] Mcdanels, D. L., 1985, "Analysis of Stress-Strain, Fracture, and Ductility Behavior of Aluminum Matrix Composites Containing Discontinuous Silicon-Carbide Reinforcement," Metall Trans A, 16(6), pp. 1105-1115.

[2] Manahan, M. P., Argon, A. S., and Harling, O. K., 1982, "The Development of a Miniaturized Disk Bend Test for the Determination of Post-Irradiation Mechanical-Properties," J Nucl Mater, 103(1-3), pp. 1545-1550.

[3] Manahan, M. P., 1983, "A New Post-Irradiation Mechanical-Behavior Test - the Miniaturized Disk Bend Test," Nucl Technol, 63(2), pp. 295-315.

[4] Norris, S. D., and Parker, J. D., 1996, "Deformation processes during disc bend loading," Materials Science and Technology, 12(2), pp. 163-170.

[5] Mao, X. Y., and Takahashi, H., 1987, "Development of a Further-Miniaturized Specimen of 3 Mm Diameter for Tem Disk (Phi-3 Mm) Small Punch Tests," J Nucl Mater, 150(1), pp. 42-52.

[6] Finarelli, D., Roedig, M., and Carsughi, F., 2004, "Small punch tests on austenitic and martensitic steels irradiated in a spallation environment with 530 MeV protons," J Nucl Mater, 328(2-3), pp. 146-150.

[7] Rodriguez, C., Cardenas, E., Belzunce, F. J., and Betegon, C., 2013, "Fracture Characterization of Steels by Means of the Small Punch Test," Exp Mech, 53(3), pp. 385-392.

[8] Garcia, T. E., Rodriguez, C., Belzunce, F. J., and Suarez, C., 2014, "Estimation of the mechanical properties of metallic materials by means of the small punch test," J Alloy Compd, 582, pp. 708-717.

[9] Giddings, V. L., Kurtz, S. M., Jewett, C. W., Foulds, J. R., and Edidin, A. A., 2001, "A small punch test technique for characterizing the elastic modulus and fracture behavior of PMMA bone cement used in total joint replacement," Biomaterials, 22(13), pp. 1875-1881.

[10] Bulloch, J. H., 2004, "A study concerning material fracture toughness and some small punch test data for low alloy steels," Eng Fail Anal, 11(4), pp. 635-653.

[11] Wang, Z. X., Shi, H. J., Lu, J., Shi, P., and Ma, X. F., 2008, "Small punch testing for assessing the fracture properties of the reactor vessel steel with different thicknesses," Nucl Eng Des, 238(12), pp. 3186-3193.

[12] Fleury, E., and Ha, J. S., 1998, "Small punch tests to estimate the mechanical properties of steels for steam power plant: I. Mechanical strength," Int J Pres Ves Pip, 75(9), pp. 699-706.

[13] Egan, P., Whelan, M. P., Lakestani, F., and Connelly, M. J., 2007, "Small punch test: An approach to solve the inverse problem by deformation shape and finite element optimization," Comp Mater Sci, 40(1), pp. 33-39.

[14] Campitelli, E. N., Spatig, P., Bonade, R., Hoffelner, W., and Victoria, M., 2004, "Assessment of the constitutive properties from small ball punch test: experiment and modeling," J Nucl Mater, 335(3), pp. 366-378.

[15] Sunjaya, D., Wei, T., Harrison, R., and Yeung, W. Y., 2007, "Finite element modelling of small punch test on 304H stainless steel," Key Eng Mat, 345-346, pp. 1165-1168.

[16] Cuesta, I. I., Alegre, J. M., and Lacalle, R., 2010, "Determination of the Gurson-Tvergaard damage model parameters for simulating small punch tests," Fatigue Fract Eng M, 33(11), pp. 703-713.

[17] Zhou, Z. X., Zheng, Y. Y., Ling, X., Hu, R. M., and Zhou, J. Q., 2010, "A study on influence factors of small punch creep test by experimental investigation and finite element analysis," Mat Sci Eng a-Struct, 527(10-11), pp. 2784-2789.

[18] Malygin, G. A., 2000, "Acoustoplastic Effect and the Stress Superimposition Mechanism," Physics of the Solid State, 42(1), pp. 72-78.

[19] Laurent, V., Jarry, P., Regazzoni, G., and Apelian, D., 1992, "Processing-Microstructure Relationships in Compocast Magnesium/Sic," J Mater Sci, 27(16), pp. 4447-4459.

[20] Saravanan, R. A., and Surappa, M. K., 2000, "Fabrication and characterisation of pure magnesium-30 vol.% SiCP particle composite," Mat Sci Eng a-Struct, 276(1-2), pp. 108-116.

[21] Harnby, N., 1984, "Trends in Powder Mixing," Chem Eng-London(405), pp. 22-23.

[22] Girot, F. A., Albingre, L., Quenisset, J. M., and Naslain, R., 1987, "Rheocasting Al Matrix Composites," Jom-J Min Met Mat S, 39(11), pp. 18-21.

[23] Zhou, W., and Xu, Z. M., 1997, "Casting of SiC reinforced metal matrix composites," Journal of Materials Processing Technology, 63(1-3), pp. 358-363.

[24] Cai, Y., Tan, M. J., Shen, G. J., and Su, H. Q., 2000, "Microstructure and heterogeneous nucleation phenomena in cast SiC particles reinforced magnesium composite," Mat Sci Eng a-Struct, 282(1-2), pp. 232-239.

[25] Ferkel, H., and Mordike, B. L., 2001, "Magnesium strengthened by SiC nanoparticles," Mat Sci Eng a-Struct, 298(1-2), pp. 193-199.

[26] Zarinejad, M., and Drew, R. A. L., 2002, "Second phase evolution in a yttria-sintered aluminum nitride ceramic," Mater Sci Forum, 383, pp. 55-67.

[27] Idris, J., and Tan, J. C., 2000, "Wear resistance property and microstructure of magnesium AZ91 composite," Magnesium Technology 2000, pp. 311-317.

[28] Wu, K., Zheng, M. Y., Yao, C. K., Sato, T., Tezuka, H., Kamio, A., and Li, D. X., 1999, "Crystallographic orientation relationship between SiCw and Mg in squeeze-cast SiCw/Mg composites," J Mater Sci Lett, 18(16), pp. 1301-1303.

[29] Chadwick, G. A., and Bloyce, A., 1992, "Squeeze Cast Magnesium Alloys and Magnesium Based Composites," Magnesium Alloys and Their Applications, pp. 93-100.

[30] Mortensen, A., and Llorca, J., 2010, "Metal Matrix Composites," Annual Review of Materials Research, Vol 40, D. R. Clarke, M. Ruhle, and F. Zok, eds., pp. 243-270.

[31] Bastwros, M., and Kim, G.-Y., 2015, "Fabrication of Aluminum–SiC Laminate Nanocomposite by Ultrasonic Spray Deposited Sheet Bonding1," Journal of Micro and Nano-Manufacturing, 3(3), pp. 031005-031005.

[32] Chen, L. Q., and Yao, Y. T., 2014, "Processing, Microstructures, and Mechanical Properties of Magnesium Matrix Composites: A Review," Acta Metall Sin-Engl, 27(5), pp. 762-774.

[33] Tay, T. E., Liu, G., Tan, V. B., Sun, X. S., and Pham, D. C., 2008, "Progressive Failure Analysis of Composites," Journal of Composite Materials.

[34] Flatscher, T., Wolfahrt, M., Pinter, G., and Pettermann, H. E., 2012, "Simulations and experiments of open hole tension tests – Assessment of intra-ply plasticity, damage, and localization," Composites Science and Technology, 72(10), pp. 1090-1095.

[35] Zhao, L., Zhi, J., Zhang, J., Liu, Z., and Hu, N., 2016, "XFEM simulation of delamination in composite laminates," Composites Part A: Applied Science and Manufacturing, 80, pp. 61-71.